High Time Resolution Structures in Radio Pulsar Emission

Dipanjan Mitra

National Centre for Radio Astrophysics, TIFR, Pune, India; email: dmitra@ncra.tifr.res.in

and

Mihir Arjunwadkar

Centre for Modeling and Simulation, University of Pune, Pune, India; email: mihir@cms.unipune.ac.in

and

Joanna M. Rankin

University of Vermont, Burlington, VT 05405 USA; email: Joanna.Rankin@uvm.edu

ABSTRACT

The bright single-pulse emission of many radio pulsars show rapid intensity fluctuations called microstructures when observed with time resolutions of some tens of microseconds. In this paper, we report Arecibo 59.5μsec-resolution polarimetric observations of 11 pulsars at 327 MHz and 32 pulsars at 1170 MHz lying in the period (P) range of 150 msec to 3.7 sec. The higher frequency observations provide the most complete basis for detailed microstructure study. On close inspection of the individual pulses, we find that most exhibit quasiperiodic structure with a periodicity P_μ. We find many examples of microstructures with deep regular modulations of the signal, but the majority appear as low level modulation on broad smooth subpulse features, and hence their periodicities are difficult to infer. In order to investigate these low level fluctuations, we developed a new analysis technique wherein each subpulse is first de-noised and then the smooth subpulse envelope subtracted. These fluctuating portions of each pulse or subpulse are then used to find P_μ by autocorrelation analysis.

Applying this analysis to all the Stokes parameters of the signal, we find that P_μ is common to the overall polarized signal. We did not find any clear signature of curvature radiation in vaccum in highly resolved microstructures. The observational analysis further shows a strong correlation between the microstructure periodicity and the pulsar period. We discuss the implications of this result in terms of a coherent radiation model, wherein the radio emission arises due to the formation and acceleration of electron-positron pairs in an inner vaccum gap (IVG) that exists above the magnetic polar cap. A subpulse in this model corresponds to a series of non-stationary sparking discharges. We argue that in such a model P_μ reflects the temporal modulation of non-stationary plasma flow.

Subject headings: MHD — plasmas — pulsars: general, radiation mechanism: nonthermal

1. Introduction

Soon after the discovery of pulsars, Craft et al. (1968) noticed submillisecond (*i.e.,* hundreds of microseconds) intensity structures in single pulses of PSR B0950+08. Subsequently several high time resolution studies revealed rapid intensity variations superposed on the subpulses of several other pulsars. This phenomenon, usually known as pulsar microstructure, is currently thought to be associated closely with the mechanisms of magnetospheric radio emission. Observationally, microstructures are found to occur simultaneously over a very wide band (*e.g.,* Rickett et al. 1975) and in pulsars with rotation periods down to 70 msec (Kramer et al. 2002), providing strong empirical evidence in favour of magnetospheric emission. The high brightness temperatures observed in pulsars rule out any thermal plasma processes, and indicate that the underlying mechanism must be a "coherent" plasma process. However, a coherent radiation mechanism that includes a physical interpretation of microstructure behaviour is yet to be identified.

In general, two appealing scenarios have been considered to explain microstructure emission, commonly known as angular beaming or temporal modulation. The angular beaming scheme is a geometrical phenomenon wherein the intensity fluctuations result from an angular radiation pattern (mimicking the microstructure width and periodicity) existing in the transverse direction. As the pulsar rotates, an observer then samples this emission structure. The temporal modulation on the other hand, entails intensity fluctuation of the propagating waves in the magnetosphere that finally reach the observer.

The existing microstructure studies fall into two broad categories: those with very high time resolutions of about 100 nanoseconds which are needed to study narrow microstructures; and those with coarser resolutions of 10 or more μsec that are useful for exploring the properties of broad microstructures. Among the former is the well known detection of ultrafast 2-nanosecond temporal structures in the Crab pulsar (Hankins et al. 2003; see also Jessner et al. 2010). Intensity fluctuations with time scales as small as 2.5μsec have also been reported in PSR B1133+16 by Bartel & Hankins (1982), and Popov et al. (2002) find micropulses with widths between 2 and 7 μsec in pulsars B0950+08, B1133+16 and B1929+10. Most of the other well known microstructure studies were geared to study the broad microstructures. These have shown that subpulses often show quasiperiodic intensity variations with periods of hundreds of microseconds (*e.g.,* Hankins 1971; Boriakoff 1976; Soglasnov et al. 1981; Soglasnov et al. 1983; Cordes et al. 1990). Cordes (1979) and Kramer et al. (2002) further show that the measured temporal width (t_μ) of a micropulse is related linearly to the rotation period P approximately as $t_\mu \sim 10^{-3}P$. Polarized microstructure has been investigated for only a few pulsars (Ferguson & Seiradakis 1978; Cordes 1979), and only for the Vela pulsar B0833–45 does some quantitative description exist (Kramer et al. 2002). Further observations, analyses and phenomenological assessments are needed to establish how microstructure

is connected physically with the mechanisms of pulsar emission.

One of the difficulties in using the existing microstructure studies to amalgamate with pulsar emission theories is that they represent different resolutions, frequencies of observation and analysis methods. Hence, in the remainder of our work, our main effort is to (1) carry out a systematic, single-frequency, single instrument (Arecibo) study of the properties of broad polarized microstructure; and (2) study the physical implications of the microstructure characteristics in the context of currently favoured coherent radio emission theories.

2. Observations

High time resolution single-pulse polarimetry observations were carried out using the Arecibo telescope for 32 pulsars at 1170 MHz (L band), and 11 pulsars at 327 MHz (P band). For these observations, we used the Observatory's Mock spectrometers in the "single-pixel" polarimetry mode. These Fourier-transform-based instruments are capable of sampling at $\sim$59.5 μsec rate and producing Stokes spectra in a filterbank format. The details of the observations are given in Table 1. This moderate time resolution was chosen both as suitable for investigating broad microstructure and maximizing the number of objects that could be so observed. In the remainder of this paper, we will then use the word microstructure to imply broad microstructure unless specified otherwise. Heretofore, only some 13 well known bright pulsars have been subjected to microstructure studies (see Table 2 of Kramer et al. 2002), out of which 11 are in the Arecibo declination range. Our sample then included all 11 of these previously studied objects at L band as well as 21 others that are now accessible owing to both the Gregorian feed system and capacious Mock backends. At P band, there is an overlap with 6 pulsars; however, for most pulsars at this frequency (apart from B1929+10), either the dispersion or the scattering timescale is comparable with the sampling rate and hence they are not suitable for microstructure study. Nonetheless, given the novelty of this 59.5-μsec polarimetry with excellent signal to noise (S/N) ratio, we do display their properties below. The high time resolution average polarization profiles for pulsars at both P band and L band are shown in Sec. A.5. Note, then, that the P band observations will therefore not be included in the analyses below or discussed therein.

The average pulsar polarization properties of the pulsars in our study agree with the lower resolution observations reported in several other studies (*e.g.*, Everett & Weisberg 2001). None of these average profiles show any obvious signature of microstructures and are consistent with the view that at any given longitude the averaging process washes out any such structure that is seen in individual pulses.

Single pulses, however, exhibit highly complex structures, with intensity fluctuations on time scales much smaller than the widths of their subpulses. Some obvious conclusions can be drawn based simply on visual inspection individual pulses. For example, we find that in several pulsars there are occasional bright pulses where the subpulses show a highly modulated or ringing structure

with all the Stokes parameters fluctuating with the same periodicity. Several such examples are shown in Fig. 1. However, almost all subpulses show lower level periodic intensity variations superposed on a broad smooth envelope. In the subsequent sections, we will develop and apply a method of extracting microstructure periodicities for both low level and highly modulated subpulses. The microstructure emission is also seen in both the orthogonal polarization emission modes, and an example is shown in Fig. 2.

3. Estimating the microstructure timescale for an individual pulse

The focus of our analysis is on extracting microstructure timescales from time-series data for individual pulses. Timescales are traditionally identified as minima, maxima, or slope changes in the autocorrelation function (ACF) for a pulse. We define the (normalized) ACF at lag τ for a signal $I(t)$ as

$$\mathrm{ACF}(\tau) = \frac{\int I(t)I(t+\tau)dt}{\int I^2(t)dt}, \tag{1}$$

so that $\mathrm{ACF}(0) = 1$. The behaviour of the ACF needs a closer look to understand what can and cannot be inferred about the timescales of a signal. For illustration, consider the toy train of Gaussian spikes (Fig. 3) which is characterized by two timescales; namely, the baseline width t_μ of each spike, and the distance between two successive spikes, $i.e.,$ the period P_μ of the spike train. The gap $g = P_\mu - t_\mu$ between two successive spikes is assumed to be non-negative. When $t_\mu \leq g$, it can be argued that the first ACF minimum occurs at lag $= t_\mu$ and the first ACF maximum occurs at lag $= P_\mu$. On the other hand, when $g > t_\mu$, successive minima and maxima in the ACF are separated by the period P_μ of the spike train. In this regime, the ACF carries no information about the width of a spike, and we expect that the lag at the first maximum $(i.e., P_\mu) = 2 \times$ the lag at the first minimum $(i.e., t_\mu)$. Conversely, any indication of the relationship $P_\mu = 2 \times t_\mu$ in the inferred timescales may therefore be interpreted as suggesting the lack of complete information about the two timescales.

To motivate the methodology we are about to develop for inferring microstructure timescales from individual subpulses in a pulsar data set, consider four illustrative subpulses from PSR B0525+21 together with their ACFs (Fig. 4). In the left column of this figure, black curves represent probable candidates for the signal in the data time series (gray scatter), red curves represent probable candidates for the smooth trend $(i.e., envelope)$ in the pulse, and blue curves represent probable candidates for the microstructure (obtained after removing the probable envelope from the probable signal). In the right column of this figure, the gray curves represent the ACF for the whole-pulse data, whereas the blue curves represent the ACF for the microstructure feature. Note that while the ACF for the whole-pulse data must be non-negative at all lags (because pulse data is by-and-large positive, barring noise), the ACF for the microstructure feature may be negative (because the microstructure signal fluctuates on both sides of 0). The time series for pulse 179 shows strong microstructure oscillations superimposed on top of a smooth envelope, which trans-

late into weak but clear oscillations in the descending part of the subpulse ACF close to lag 0. For this pulse, we see that the first minimum in the subpulse ACF (gray curve in the ACF plot) agrees with the first minimum in the ACF for the microstructure feature (blue curve in the ACF plot). This pulse is an example where the conventional method of identifying microstructure timescales using the first minimum in the ACF will work flawlessly because the first minimum in the subpulse ACF is numerically well-defined. The time series for pulse 37 again shows a highly fluctuating signal characteristic of the microstructure. However, the first ACF minimum is barely visible in the subpulse ACF. In contrast, the first minimum is clearly identifiable in the microstructure ACF for this pulse. The time series for pulse 21 again shows a clearly identifiable microstructure feature. However, it nevertheless leads to a featureless subpulse ACF which makes it impossible for the conventional method to identify a microstructure timescale from it. The ACF for the microstructure feature, in contrast, has a clearly identifiable first minimum. Pulse 62 is an example where, with the exception of one or two clear but weak fluctuations in the time series, there may not be any significant/detectable microstructure feature.

These illustrative pulses suggest that the signal hidden in the data can be modeled as consisting of an *envelope* feature characterized by relatively strong long-time smooth variations, and a *microstructure* feature characterized by relatively weak short-time quasiperiodic variations that ride on top of the envelope. Hence, with reference to the use of ACFs for identifying timescales, we expect the following two confounding situations:

1. The ACF of the complete pulse may be dominated by power at low frequencies, *i.e.,* by the envelope feature, possibly masking any short-time modulations (*e.g.,* pulses 37 and 36 in Fig. 4).

2. Noise in the data may result in additional random oscillations in the ACF, making it numerically difficult to identify genuine minima, slope changes, etc., in the ACF.

This suggests that if the noise and the envelope feature are extracted from the data to arrive at the microstructure feature, then it can be used meaningfully to estimate microstructure timescales from the ACF in the conventional manner.

Therefore, a solution to the problem of estimating microstructure timescales lies in correctly estimating and removing the noise as well as the long-time smooth modulation (*i.e.,* envelope) from a subpulse time series. Our methodology for estimating microstructure timescales from individual subpulses thus consists of the following steps.

1. The average pulse profiles for many pulsars are often seen to be composed of multiple emitting components. As was pointed out in some earlier studies (*e.g.,* Soglasnov et al. 1981; Soglasnov et al. 1983; Popov et al. 2002), the individual components can have different microstructure timescales. Hence, we isolate individual pulse components wherever possible before estimating timescales. Individual components are identified from the average pulse profile in the form of

time windows relative to the beginning of the profile. These windows are then used on each single pulse in the data set to separate it into its components. For pulsars where multiple components could not be identified, we used whole pulses. Further, we restrict our analysis only to pulses with high S/N, where S/N is estimated as the ratio of the peak signal to the off-pulse noise. In Table 1, the pulsars marked in bold face are the ones with sufficient single-pulse S/N and hence were suitable for timescale analysis, while the others are not used.

2. RFI-induced outlier values in subpulse time series data may influence timescale estimates. We therefore identify potential outliers in subpulse time series data using a heuristic method, and replace them with appropriate values resembling their respective local environments in the time series (Sec. A.2). The decision to "curate" outliers is made on a case-to-case basis through preliminary visual inspection of each pulsar data set.

3. We de-noise every subpulse using a model-independent smoothing spline fit (Sec. A.3) that adapts to the shape of the subpulse optimally. The fit thus obtained is a smooth noise-free version of the subpulse data (*e.g.,* the black curves in Fig. 4 left column).

4. We estimate the envelope for each subpulse via kernel regression (Sec. A.4) using a heuristic smoothing timescale. The difference between the fit and this envelope is the estimated microstructure. Further details can be found in Sec. 4.

5. The nature and strength of the microstructure feature can vary considerably among subpulses. Specifically, the microstructure feature may be nearly absent or at best weak in some of the subpulses. We identify subpulses with weak microstructure using the *degrees of freedom* (DF) for the smoothing spline fit (Sec. A.3), because lower DF values correspond to smoother fits and weaker microstructures. For better estimation of microstructure timescales, we reject subpulses with DF in the lower 10-20 percentiles of the DF distribution for that data set (See Supplementary Table 1 for the percentile cut-off for each data set).

6. For the selected pulses, the two characteristic microstructure timescales (width t_μ and period P_μ) are estimated respectively as the first minimum and the first maximum in the ACF of the estimated microstructure for a subpulse. Because of the substantial variation in microstructure characteristics across subpulses, the timescales thus obtained need to be further summarized or analyzed statistically. Specifically, for each pulsar, we report the median timescale together with the median absolute deviation (MAD) as a measure of the spread. We also explore the nature of any relationship between t_μ and P_μ.

The microstructure timescale analysis pipeline developed in this paper is implemented in the R (R Core Team 2014) open source statistical computing environment [1]

---

[1]Detailed pulsarwise results is available as a tarball in: `ftp://wm.ncra.tifr.res.in/dmitra/hires_analysis_pdf.tar.gz`

4. Results

Fig. 5 and 6 depict typical results from our analysis package. Fig. 5 shows how the technique is applied to a subpulse (see caption for description). We estimate the microstructure periodicity P_μ as the first peak in the ACF of the microstructure signal (blue line), and show the results for three envelope smoothing bandwidths h because the estimated timescales are sensitive to the envelope bandwidth, where h is the smoothing window size in units of the total number of points in a subpulse (see Sec. A.4 for details). In the absence of any theoretical prediction for microstructure timescales, it is difficult to choose an appropriate value for h from first principles. Hence, we used crucial properties of the data along with estimated timescales from earlier microstructure studies in the literature to converge on a range of h values. For every pulsar, we identified a few highly fluctuating/modulating pulses (like examples shown in Fig. 1) where the P_μ estimated from first peak in the ACF is easily discernible. This gave us a range of h values over which the P_μ value remained unchanged. Using a few representative h values in this range we found the distributions of P_μ. The median value of these P_μ distribution (or t_μ found from first dip in the ACF) appeared to be in good agreement for pulsars where such estimates exist in the literature. We found that for all pulsars, h larger than 0.1 produced envelopes that were too smooth, whereas h less than 0.05 led to envelopes that traced the subpulse data too closely. All our results are hence quoted for three representative bandwidths, namely, 0.1, 0.075 and 0.05, as illustrated in Fig. 6. The median of the P_μ histogram is given in columns 4, 5 and 6 of Table 2 where the spread of the P_μ distribution is characterized in terms of the median absolute deviation (MAD). Column 2 gives the longitude range used to define the subpulses for microstructure analysis, and these can be identified from the average pulse profiles presented in Sec. A.5.

The top panel of each plot in Fig. 6 deserves attention. The plot depicts the relationship between the values of the first dip (or t_μ) along the x-axis and the first peak (or P_μ) along the y-axis as estimated from the ACFs of the microstructure. The three dotted lines correspond to $P_\mu = t_\mu, P_\mu = 2t_\mu$ & $P_\mu = 4t_\mu$, respectively. Most of the points in this figure (and also for other pulsars) are seen to cluster around the $P_\mu = 2t_\mu$ line, indicating that the microstructure is unresolved and hence the width t_μ cannot be determined.

Before we close this section it is important to compare our analysis method with earlier studies. The majority of the studies use the first dip or peak of the ACF to estimate microstructure timescales (*e.g.,* Soglasnov et al. 1981; Hankins 1972). However, as mentioned earlier, the broad subpulse power as well as noise in the subpulse makes it difficult to extract the time scales numerically. Our method is designed to alleviate these problems by first de-noising the subpulse profile, and then taking out a smooth envelope from it. Other studies have used the power spectrum route to estimate timescales corresponding to quasiperiodic microstructures (*e.g.,* Popov et al. 2002; Lange et al. 1998). The slow-varying envelope in these cases appears as low-frequency power in the spectrum. To address this problem Popov et al. (2002) constructs the ACF by cross-correlating the voltages from two different spectral channels, while Lange et al. (1998) use the derivative of the power spectrum, although the noise in the single pulses still affects their analyses. The strength of

our current study, on the other hand, is its ability to recover low level intensity modulation as microstructure in subpulses. Consequently we find that majority of the subpulses have microstructure emission superposed on a smooth broad emission (envelope).

5. Distribution of timescales for all Stokes parameters and the P_μ-P relation

Cordes (1979), based on 10 pulsars observed at 430 MHz in the pulsar period range of 0.2 to 3.7 second, found the relationship $t_\mu \sim 10^{-3} P$ between the microstructure timescale t_μ and the pulsar period P. Kramer et al. (2002) reestablished this relationship as $t_\mu(\mu s) \sim (600 \pm 100) P(s)^{1.1 \pm 0.2}$ using 12 pulsars where t_μ estimates were available in the literature for different frequencies. With our current set of observations we are in a position to revisit this relationship using 24 pulsars at L Band. Since broad microstructures cannot be resolved, we believe that the periodicity P_μ is a more relevant quantity instead of t_μ. Fig. 7 plots the the median value of P_μ against period P. The top panel corresponds to the total intensity, the middle one to the linear polarization, and the bottom one to the circular. The P_μ points are estimated from the median value of the histogram of the first peak in the ACF, and the error bars reflect the median absolute deviation of the P_μ distribution. A linear fit to the median P_μ gives $P_\mu(\text{msec}) \sim 0.11 + 1.1 \times 10^{-3} \text{P (msec)}$. We note that the fit is merely demonstrating the tendency that median P_μ increases with increasing pulsar period, although a large spread of P_μ's exists for all pulsars.

6. How does broad microstructure average to form a subpulse?

It was evident from early polarization observations (*e.g.,* Clark & Smith 1969; Manchester et al. 1975) that single pulses are highly linearly polarized and the circular polarization changes sign or handedness within a pulse. More recently Mitra et al. (2009, hereafter MGM09), based on high quality single-pulse polarimetry, clearly showcased a collection of subpulses from an assorted set of pulsars, where the subpulses had a Gaussian shape, with close to 100% linear polarization and associated with sign-changing circular. One such example is shown in the left panel of Fig. 8.

For a long time this emission pattern kindled great interest in the pulsar community (see *e.g.,* Michel 1987; Radhakrishnan & Rankin 1990), as this remarkably resembles the emission pattern due to single-particle vaccum curvature radiation as the observer cuts across the emission cone (*i.e.,* the $1/\gamma$ cone). The mathematical foundation for obtaining Stokes parameters due to curvature radiation in vaccum for a single relativistically moving particle has been explicitly calculated by several authors (*e.g.,* Gil & Snakowski 1990b; Gil & Snakowski 1990a; Ahmadi & Gangadhara 2002). Let us recall the polarization properties of single-particle curvature radiation in vaccum based on the description given by Gil & Snakowski (1990a,b). Consider a charged particle moving relativistically with a lorentz factor γ, along superstrong magnetic field lines, with a radius of curvature ρ. The particle will emit curvature radiation beamed in the forward direction. The

Fourier components of the electric fields can be decomposed into parallel ($\varepsilon_\parallel$) and perpendicular ($\varepsilon_\perp$) components to the plane of the curved magnetic field lines (see eqs. 7 and 8 of Gil & Snakowski 1990a). When the radiation is viewed as a cut through the emission beam, the $\varepsilon_\perp$ has a sinusoidal form, $\varepsilon_\parallel$ is positive and has a relative phase-shift of 90° forming an orthogonal basis. The radiation polarized in the parallel and perpendicular direction are also known as the ordinary (O) and extraordinary (X) modes. The power in curvature radiation is dependent on the frequency of emission, and it achieves its maximum at ν_c, the characteristic frequency which is given by the expression $\nu_c = 1.25\gamma^3\nu_0$ in the vaccum case (See fig. 2 of Gil & Snakowski 1990b). The ratio of the two components as well as the width of the pulse is dependent both on the viewing angle φ and the frequency of emission (see figs. 3, 4 and 5 of Gil & Snakowski 1990b). The width of the pulse is approximately equal to $\delta = 1/\gamma$ at ν_c. The power in the O mode is seven times stronger than the X mode in vaccum (Jackson 1975; Gil et al. 2004).

Our purpose here is to find signatures of the aforementioned vaccum curvature radiation in the data. First let us note that the subpulse width cannot be associated with the elementary $1/\gamma$ emission cone, since when observed with higher time resolution, the subpulse splits into microstructures. In an attempt to reproduce this subpulse radiation pattern, Gil & Snakowski (1990a) and Gil et al. (1993) used the shot-noise model of pulsar emission, where the subpulse is an incoherent addition of smaller bunches, with each bunch emitting like a single-particle vaccum curvature radiation. The subpulse shape results from the intensity gradient due to the charge density variation of the bunches across the subpulse. The authors demonstrated that in the presence of intensity gradients, the resulting emission will have a net circular polarization as observed in subpulses. The beams from the bunches do not overlap, so the linear polarization remains high. Assuming $\gamma \sim 100$, and therefore an angular size $1/\gamma \sim 0.6°$ for the emitting bunches, they simulated several pulses that appear similar to the subpulses showcased by MGM09. These results were also recently confirmed by Gangadhara (2010). A prediction of this model is that if a subpulse can be resolved into microstructures (e.g., see fig. 3 of Gil et al. 1993), then the microstructure should have features which mimic the single-particle vaccum curvature-radiation pattern. To test this theory we need examples of subpulses where the microstructures are highly resolved. Note that the subpulses chosen should be highly linearly polarized such that they do not suffer from any depolarization effects due to orthogonal polarization moding[2] or due to incoherent addition from overlapping $1/\gamma$ emission beam (see MGM09).

In the left hand panel of Fig. 8 a subpulse of PSR B2020+28 is shown which is highly linearly polarized and is associated with a sign-changing circular polarization, similar to the pulses showcased by MGM09. The right hand panel shows the high time resolution data for the same

---

[2]It is important to touch upon a subtle point regarding sign-changing circular polarization in pulsar subpulses. In some cases at the zero-crossing point of the sign-changing circular, the linear polarization drops significantly and the PPA gets associated with an orthogonal jump. However for testing the vaccum curvature-radiation signatures, such subpulses are undesirable as they do not comply with the basic property of vaccum curvature radiation where, at the zero-crossing point of the circular, the fractional linear polarization has to be close to 100%.

subpulse, and clearly resolved microstructures are seen. As expected the linear polarization of the individual microstructures are close to 100% in order to produce the highly polarized subpulse. The circular polarization below the microstructure feature does not show any sign reversals. Rather it has the same width (and also periodicity) as the total intensity and linear polarization. In fact this description is true for all subpulses where sufficiently resolved microstructures are seen. Fig. 1 shows several such examples, and very clear examples where Stokes V has the same P_μ as Stokes I and L are shown in Fig. 9. This feature is also borne out from the statistical analysis of the data set where the median P_μ values of Stokes I, L & V are similar as can be seen in Table 2. Thus based on these observations one is compelled to conclude that radiation pattern of resolved microstructures are not consistent with single-particle curvature radiation of charged bunches in vaccum. In the next section we will discuss how these findings corroborate with our current understanding of the pulsar emission mechanism.

7. Pulsar microstructure and its implications for the coherent radio emission mechanism.

Coherent pulsar radio emission can be generated by means of either a maser or coherent curvature mechanism (Ginzburg & Zhelezniakov 1975; Kazbegi et al. 1991; Melikidze et al. 2000, hereafter MGP00). There is general agreement that this radiation is emitted in curved magnetic field-line planes due to growth of plasma instabilities in the strongly magnetized electron-positron plasma well inside the light cylinder. Many observational constrains on the emission altitude suggest that the emitted radiation detaches from the ambient plasma at altitudes of about 500 km above the stellar surface which is typically less than 10% of the light cylinder radius $R_{LC} = Pc/2\pi$ (*e.g.,* Cordes 1978; Blaskiewicz et al. 1991; Rankin 1993; Kijak & Gil 1997; Mitra & Deshpande 1999; Gangadhara & Gupta 2001; Mitra & Li 2004; Krzeszowski et al. 2009). The magnetic field at these altitudes is so strong that the plasma is constrained to move only along the magnetic field lines. Under such conditions the two-stream instability is the only known instability that can develop, and the growth of this plasma instability leads to the formation of charged relativistic solitons, which can excite the coherent curvature radiation in the plasma (*e.g.,* Asseo & Melikidze 1998; Melikidze et al. 2000; Gil et al. 2004 GLM04 hereafter).

The basic requirement of the theory of coherent radio emission is the presence of a non-stationary inner acceleration region. Ruderman & Sutherland (1975) (hereafter RS75) were amongst the first to explore the conditions in the pulsar magnetosphere that lead to the formation of an inner accelerating region (also known as an inner vaccum gap, IVG) just above the pulsar polar cap where the free flow of charge is hindered, thus resulting in the formation of an inner vaccum gap with a large potential difference. The physics of inner vaccum gap formation can be found in RS75, and here we point out that the original RS75 inner vaccum gap was not consistent with x-ray observations and radio subpulse drifting observations, and currently it is thought that a partially screened inner vaccum gap exists close to the neutron star surface (Gil et al. 2003). The process that

generates non-stationary flow of charges in the gap is as follows. The IVG is initially discharged by a photon-induced electron-positron pair-creation process in the strong curved magnetic field. The height (h_g) of the gap stabilizes typically at about a few mean-free paths of the pair-production process. The electric field in the gap causes separation of the electrons and positrons (also known as primary particles), where the electrons bombard onto the neutron-star surface, and the positrons are accelerated away toward the outer magnetosphere. As these primary particles move they accelerate and create further secondary particles resulting in a pair-creation cascade. The outflowing particles are hence composed of primary particles with Lorentz factors of about 10^6 and secondary plasma clouds with a distribution of Lorentz factors from about 10 to 1000, but peaking around 300–500. This process eventually occurs over a set of magnetic field lines, and this overall spread of the discharging process is called a spark. As the electron moves towards the polar cap it experiences $E \times B$ drift, causing the sparking discharge to move slowly across the polar cap. RS75 envisaged that the inner vaccum gap is discharged in the form closely packed isolated sparks, where the lateral size and distance between the sparks is equal to the gap height. A plasma column is associated with each spark, and in the radio-emission region coherent spark-associated plasma columns radiate and generate the observed subpulses in pulsars. The sparking process continues for a time t_s until the whole potential in the gap is screened out, after which the plasma empties the gap in a time $t_g = h_g/c$ and once again the sparking process starts almost in the same place on a time scale $\sim t_g << t_s$ (Gil & Sendyk 2000). This process results in a non-stationary flow of plasma clouds associated with every spark anchored to a specific location on the polar cap. The physics of the sparking discharge process is still a topic of active research, however most studies suggest that in normal pulsars h_g is of the order of about 50–100 m, and to screen the gap potential around 50 pair creations are needed; and hence $t_s \sim 50 h_g/c \sim 10\mu$ sec. Note that during the time t_s the $E \times B$ drift causes the spark to move only very slightly across the polar cap. Two successive plasma clouds, with each cloud extending for about $50 h_g$ and separated by a distance h_g, eventually overlap when the fast moving particles of the second cloud catch up with the slow moving particles of the first cloud, leading to the development of the two-stream instability. The instability in the plasma generates Langmuir plasma waves and the modulational instability of the Langmuir waves leads to the formation of a large number of charged solitons which can excite extraordinary (X) and ordinary (O) modes of curvature radiation in the plasma cloud as shown by MGP00 and GLM04. The condition for coherent emission requires the wavelength of emission to be greater than the intrinsic soliton size, *i.e.,* $\omega < 2\sqrt{\gamma_s}\omega_p$ where $\omega_p = (4\pi e^2 n/m_e)^2$ is the plasma frequency (see MGP00, GLM04), and γ_s is the Lorentz factor of the secondary plasma. The emerging radiation is an incoherent addition of the radiation emitted by each soliton.

We now discuss aspects of the soliton coherent-curvature radiation theory that relate to the two important microstructure behaviours discussed in this paper, namely the periodic structures observed in pulsar subpulses, their linear dependence with pulsar period and the absence of signatures of vaccum curvature radiation in pulsar microstructures. Obviously the time scales involved in the radiation process are far too small to be seen in our 59.5μsec observations, hence we rule out that the periodic microstructures correspond to emission from individual plasma clouds or

solitons[3]. Another way of sampling a periodic structure would be if temporal modulation of the emission exists in the emission region. There are theoretical studies in the literature which attempt to interpret microstructure based on nonlinear plasma effects leading to temporal modulation of the pulsar emission (*e.g.*, Chian & Kennel 1983; Weatherall 1998; Asseo 1993); however these models are mostly developed for emission where $\omega \geq 2\sqrt{\gamma_s}\omega_p$, whereas coherent emission requires $\omega < \omega_p$.

The other important aspect of our observations is the absence of a signature of vaccum curvature radiation in pulsar microstructures. The coherent curvature radiation by charged bunches called solitons excites the extraordinary and ordinary mode in the electron-positron plasma. Due to the strong ambient magnetic field the X-mode does not interact with the plasma and hence can escape the plasma and reach the observer (MGM09, Melikidze et al. 2014) . The fate of the O-mode is however unclear. It has been suggested that it can be damped and gets ducted along the magnetic field lines, or if there are sharp plasma boundaries that it can escape as electromagnetic waves and reach the observer. In any case, due to propagation effects in the plasma, the X and O modes separate in phase and hence they do not maintain any phase relation as they emerge from the plasma. As a result the circular polarization can no longer have any sign-changing signature as in the vaccum case. Also incoherent addition of a large number of solitons would tend to cancel any circular polarization, particularly in our observations. Thus the origin of circular polarization still remains to be understood in this model of pulsar emission.

8. Summary

In this work we have found several distinguishing features of pulsar microstructures. These can be summarized as follows

1. Almost all subpulses show a quasiperiodic structure riding on top of a broad pulse envelope. In general this structure is weak, except in occasional cases when deep modulations are seen. However, the absence of microstructure in pulsar average profiles is a clear indication that at any given longitude pulsar emission is random and stochastic.

2. Microstructures are also seen to be associated with both the orthogonal polarization modes.

3. We did not find any case where microstructure widths are resolved. In other words we find that $P_\mu \sim 2t_\mu$ (where the estimated width is t_μ found as the first dip in the ACF) is related to the periodicity P_μ (found as the first peak in the ACF) (see Sec. 3 for details).

4. For every pulsar the P_μ values extracted from a collection of subpulses have a distribution, and the median value of P_μ linearly increases with pulsar period (see Sec. 5).

---

[3]Note that in this context the findings of Popov *et al.* (2002) are rather interesting as based on their 62.5 nanosec observations they report that the shortest microstructure widths are about 2μs to 10μs, which corresponds to the time over which the sparking discharge takes place.

5. All the Stokes parameters have the same width and periodicity—*i.e.,* they have same P_μ values (see Sec 6).

A variety of analysis techniques to extract microstructure times scales have been deployed in the past. The methods use either the ACF first dip and first peak or use the peaks in the power spectra for estimating timescales. These methods however cannot effectively find the low level wiggles that are observed in subpulses. We address this problem by de-noising the subpulse signal and subsequently removing a broad envelope. The ACF of the resultant signal is then used to estimate microstructure timescales.

These quasiperiodic structures, which show a linear dependence on rotation period, cannot be understood in terms of the current theories of pulsar emission. We also find that the linear and circular polarization follow the same distribution of time scales as the total intensity. This, as we have argued strongly, rules out the possibility that microstructures are basic units of curvature radiation in vaccum. We conclude that the microstructures within the pulsar signal reflect temporal modulations of plasma processes of the emission engine. While this paper is an exercise to understand the properties of pulsar microstructures, theoretical progress needs to be made to understand this unique phenomenon.

9.   Acknowledgements

REFERENCES

Ahmadi, P., & Gangadhara, R. T. 2002, *Ap.J.*, 566, 365

Asseo, E. 1993, *MNRAS*, 264, 940

Asseo, E., & Melikidze, G. I. 1998, *MNRAS*, 301, 59

Bartel, N., & Hankins, T. H. 1982, *Ap.J. Lett.*, 254, L35

Blaskiewicz, M., Cordes, J. M., & Wasserman, I. 1991, *Ap.J.*, 370, 643

Boriakoff, V. 1976, *Ap.J. Lett.*, 208, L43

Chian, A. C.-L., & Kennel, C. F. 1983, Ap&SS, 97, 9

Clark, R. R., & Smith, F. G. 1969, *Nature*, 221, 724

Cordes, J. M. 1978, *Ap.J.*, 222, 1006

—. 1979, Australian Journal of Physics, 32, 9

Cordes, J. M., Weisberg, J. M., & Hankins, T. H. 1990, A.J., 100, 1882

Craft, H. D., Comella, J. M., & Drake, F. D. 1968, *Nature*, 218, 1122

Efromovich, S. 1999, Nonparametric Curve Estimation: Methods, Theory, and Applications (New York, USA: Springer)

Everett, J. E., & Weisberg, J. M. 2001, *Ap.J.*, 553, 341

Ferguson, D. C., & Seiradakis, J. H. 1978, *A&A*, 64, 27

Frigge, M., Hoaglin, D. C., & Iglewicz, B. 1989, The American Statistician, 43, pp. 50

Gangadhara, R. T. 2010, *Ap.J.*, 710, 29

Gangadhara, R. T., & Gupta, Y. 2001, *Ap.J.*, 555, 31

Gil, J., Kijak, J., & Zycki, P. 1993, *A&A*, 272, 207

Gil, J., Lyubarsky, Y., & Melikidze, G. I. 2004, *Ap.J.*, 600, 872

Gil, J., Melikidze, G. I., & Geppert, U. 2003, *A&A*, 407, 315

Gil, J. A., & Sendyk, M. 2000, *Ap.J.*, 541, 351

Gil, J. A., & Snakowski, J. K. 1990a, *A&A*, 234, 237

—. 1990b, *A&A*, 234, 269

Ginzburg, V. L., & Zhelezniakov, V. V. 1975, ARA&A, 13, 511

Green, P., & Silverman, B. 1994, Nonparametric Regression and Generalized Linear Models: A Roughness Penalty Approach (New York, USA: Chapman and Hall)

Hankins, T. H. 1971, *Ap.J.*, 169, 487

—. 1972, *Ap.J. Lett.*, 177, L11

Hankins, T. H., Kern, J. S., Weatherall, J. C., & Eilek, J. A. 2003, *Nature*, 422, 141

Härdle, W. 1992, Applied Nonparametric Regression (Cambridge, UK: Cambridge University Press)

Jackson, J. D. 1975, Classical electrodynamics

Jessner, A., Popov, M. V., Kondratiev, V. I., et al. 2010, *A&A*, 524, A60

Kazbegi, A. Z., Machabeli, G. Z., & Melikidze, G. I. 1991, *MNRAS*, 253, 377

Kijak, J., & Gil, J. 1997, *MNRAS*, 288, 631

Kramer, M., Johnston, S., & van Straten, W. 2002, *MNRAS*, 334, 523

Krzeszowski, K., Mitra, D., Gupta, Y., et al. 2009, *MNRAS*, 393, 1617

Lange, C., Kramer, M., Wielebinski, R., & Jessner, A. 1998, *A&A*, 332, 111

Manchester, R. N., Taylor, J. H., & Huguenin, G. R. 1975, *Ap.J.*, 196, 83

Melikidze, G. I., Gil, J. A., & Pataraya, A. D. 2000, *Ap.J.*, 544, 1081

Melikidze, G. I., Mitra, D., & Gil, J. 2014, ArXiv e-prints, arXiv:1409.1587

Michel, F. C. 1987, *Ap.J.*, 322, 822

Mitra, D., & Deshpande, A. A. 1999, *A&A*, 346, 906

Mitra, D., Gil, J., & Melikidze, G. I. 2009, *Ap.J. Lett.*, 696, L141

Mitra, D., & Li, X. H. 2004, *A&A*, 421, 215

Popov, M. V., Bartel, N., Cannon, W. H., et al. 2002, *A&A*, 396, 171

R Core Team. 2014, R: A Language and Environment for Statistical Computing, R Foundation for Statistical Computing, Vienna, Austria, http://www.R-project.org/

Radhakrishnan, V., & Rankin, J. M. 1990, *Ap.J.*, 352, 258

Rankin, J. M. 1993, *Ap.J.*, 405, 285

Rickett, B. J., Hankins, T. H., & Cordes, J. M. 1975, *Ap.J.*, 201, 425

Ruderman, M. A., & Sutherland, P. G. 1975, *Ap.J.*, 196, 51

Soglasnov, V. A., Popov, M. V., & Kuzmin, O. A. 1983, Soviet Ast., 27, 169

Soglasnov, V. A., Smirnova, T. V., Popov, M. V., & Kuzmin, A. D. 1981, Soviet Ast., 25, 442

Wasserman, L. 2006, All of Nonparametric Statistics (New York, USA: Springer)
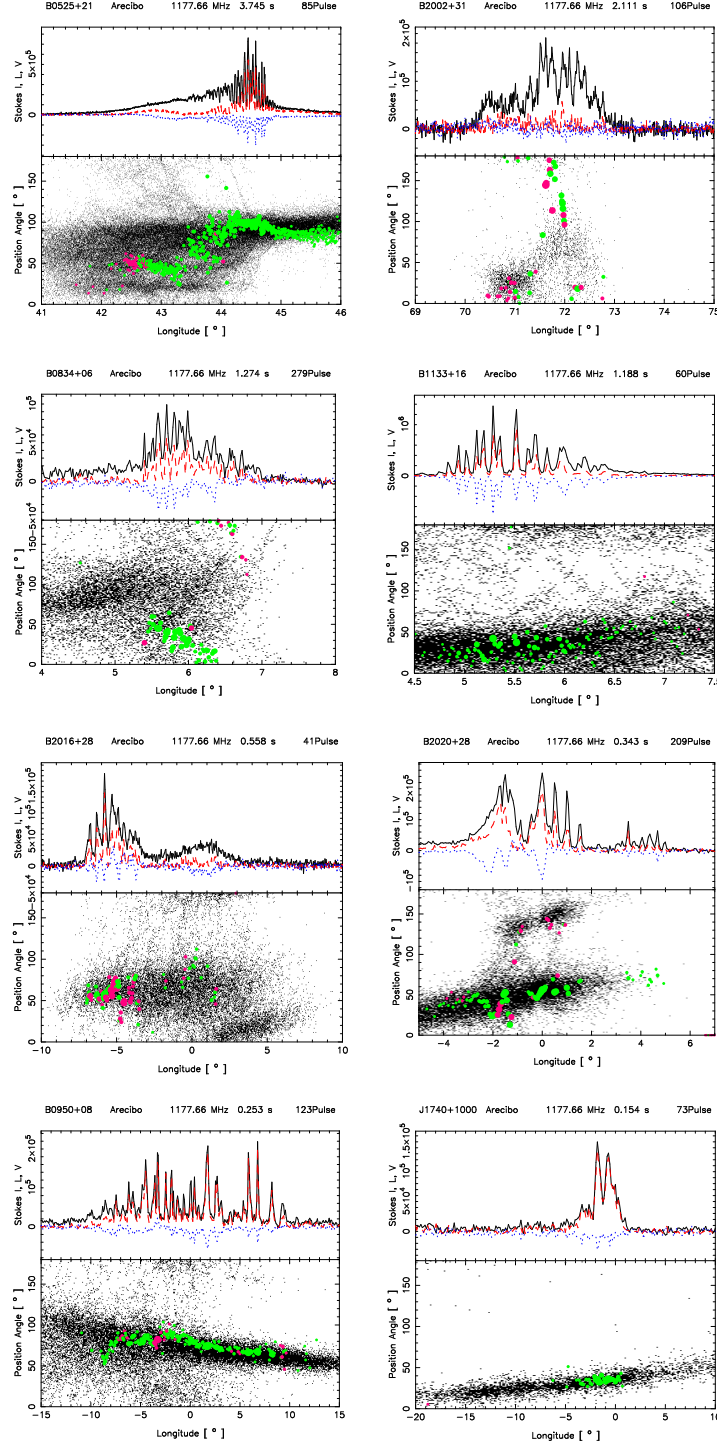
Weatherall, J. C. 1998, *Ap.J.*, 506, 341

Fig. 1.— A collection of subpulses are shown in full polarization for various of the pulsars observed with a time resolution of 59.5 μsec. In each plot the top panel shows Stokes I, L and V in black, red and blue lines respectively. The PPA histogram of the entire pulse sequence is shown as a "dotty plot" display of qualifying samples in the bottom panel. The average PPA of the subpulse is plotted in green when the circular polarization is negative and magenta when positive. The ringing/modulating structures seen in the subpulses are microstructures. Note that a certain periodicity (or quasiperiodicity) is apparent in the microstructures, and all the Stokes parameters fluctuate in the same manner with the same width and periodicity.
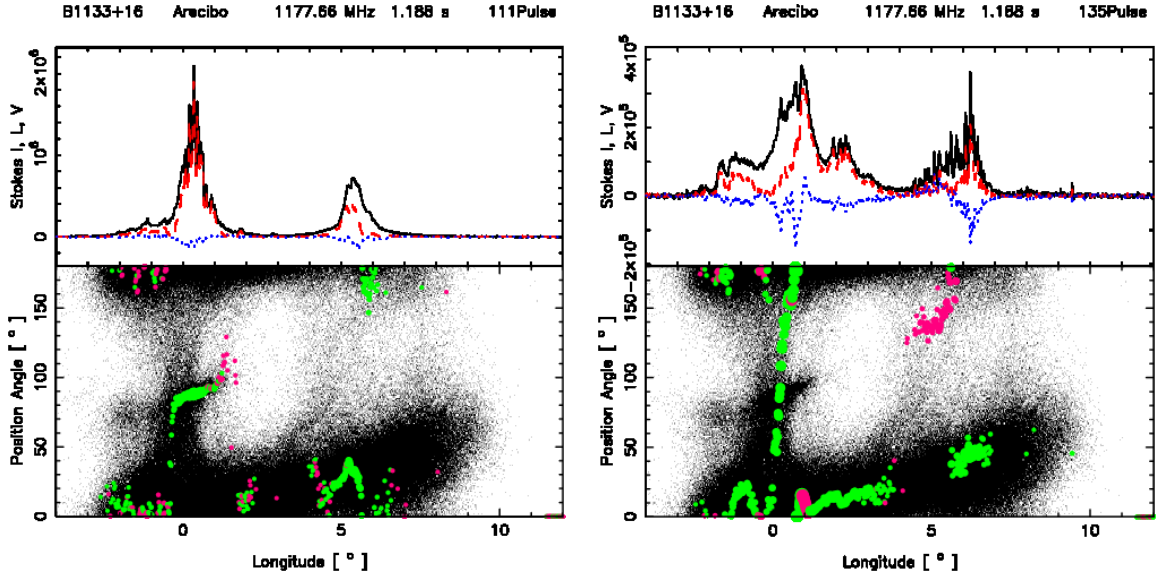
Fig. 2.— Two single pulses of PSR B1133+16 as in Fig. 1, illustrating that microstructures occur within both polarization modes. In the left hand display around 0° longitude the pulse component showing the microstructure feature corresponds to the weaker secondary polarization mode; whereas in the right hand one at about 6° the microstructure corresponds to the primary polarization mode.
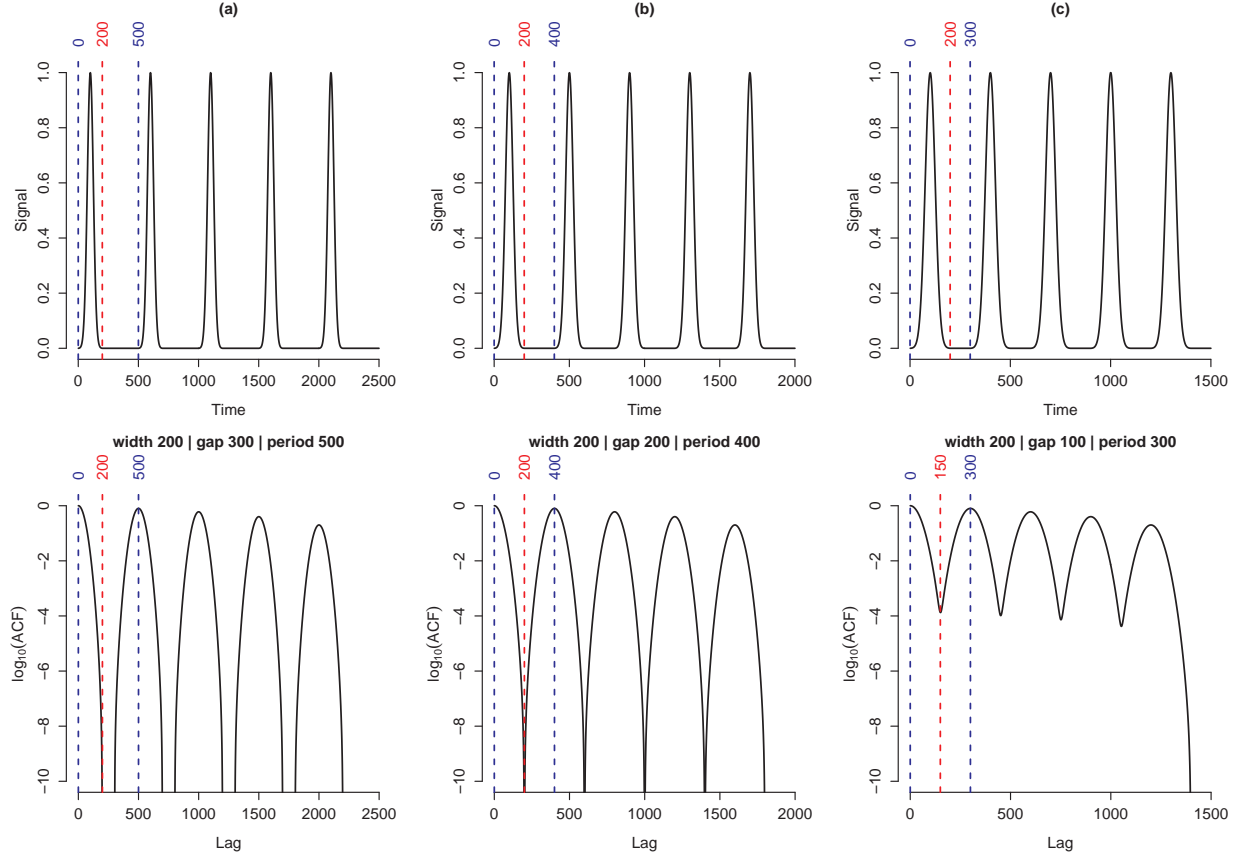
Fig. 3.— A toy example illustrating the relationship between the width of a spike, period of a spike train, and the first minimum and maximum in the ACF. In the top row, each spike is a truncated Gaussian with baseline width = 200, and the spike train is a sequence of equidistant spikes separated with the same gap. The period of the spike train therefore equals the widths of a spike + gap between successive spikes. (a) width < gap; (b) width = gap; (c) width > gap. In all cases, the first ACF maximum is at lag = period. For (a) and (b), the first ACF minimum is at lag = width, and the ACF can be used to infer both the width and period of the spike train. For (c), the first ACF minimum is at lag = period/2, and the ACF carries no information about the width. The spike train is a caricature of the microstructure feature of a subpulse, and illustrates what can be inferred about timescales using the ACF. Note that the bottom row plots $\log_{10}(\text{ACF})$ instead of the ACF so as to accentuate the ACF minima.
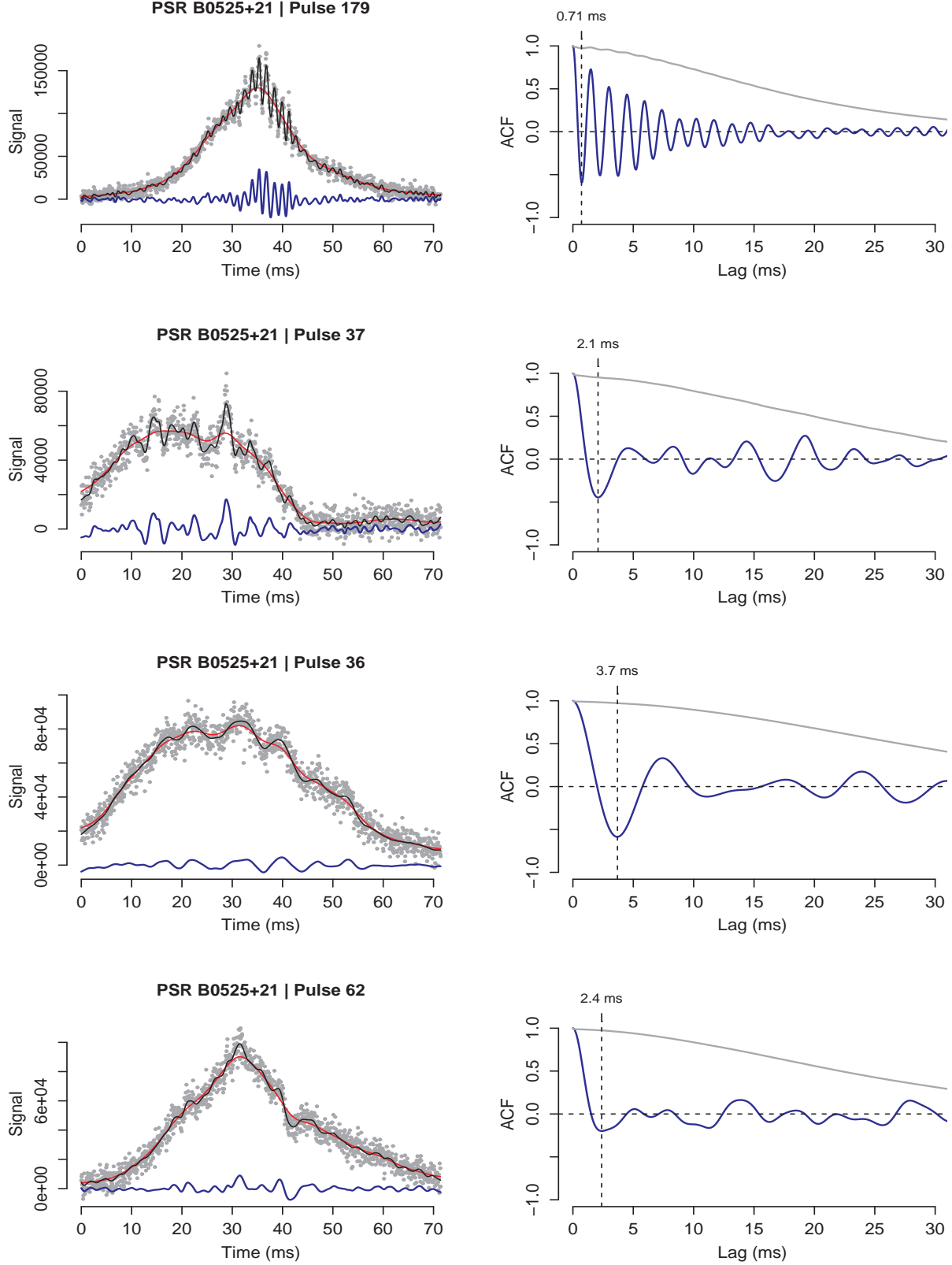
Fig. 4.— A few illustrative subpulses from a B0525+21 data set and their respective ACFs. Left column: gray, subpulse time series data; black, probable signal in the data sans the noise; red, probable smooth trend in the time series; blue, probable microstructure feature of the signal. Right column: gray, ACF computed directly from noisy data, blue: ACF computed from the probable microstructure feature. See text for detailed description.
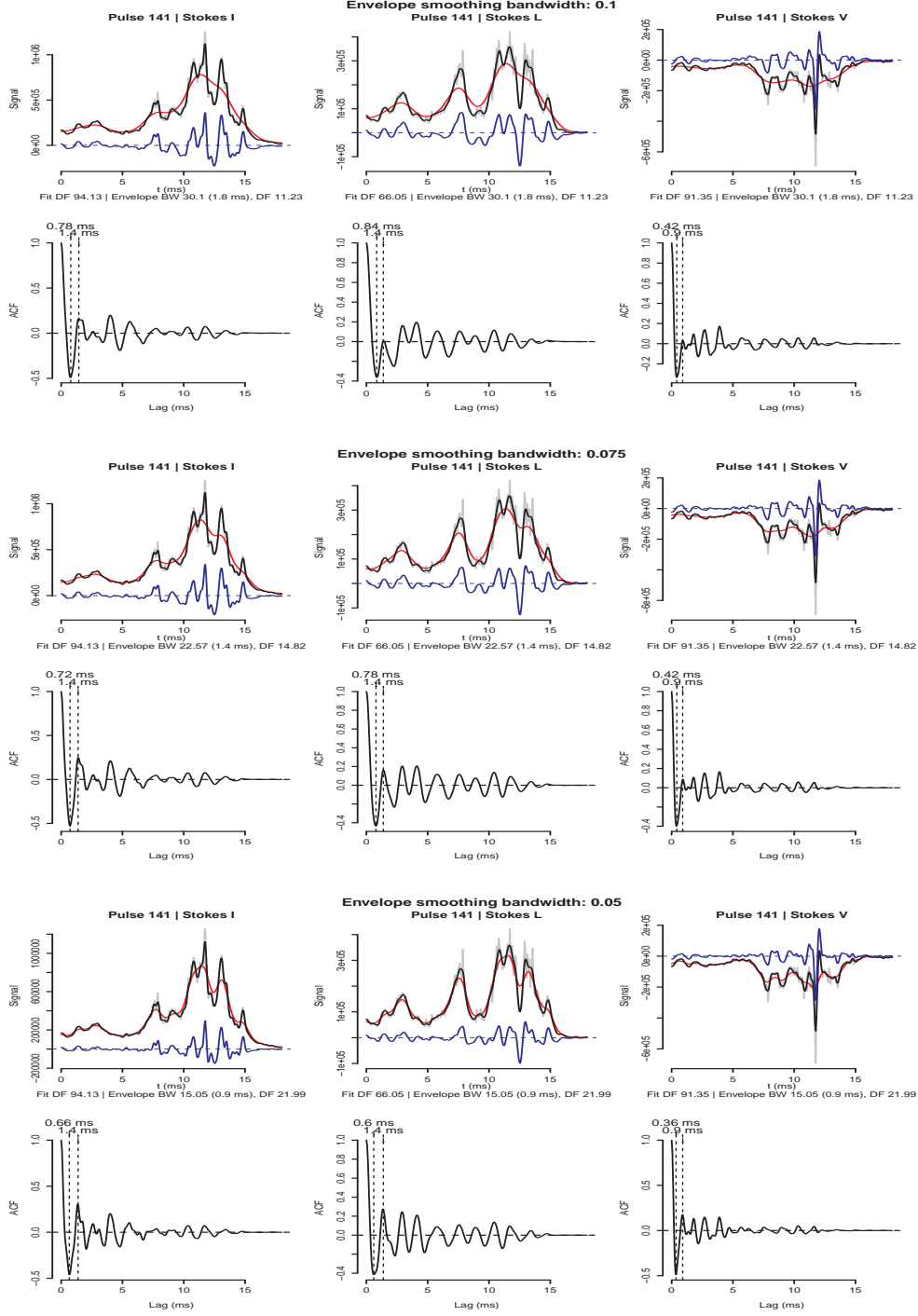
Fig. 5.— The analysis method for extracting the timescale of a single subpulse in the trailing component of PSR B1133+16 is illustrated in this figure. The plot has three columns, with each column corresponding to Stokes I, L and V, respectively. In each column the upper panel shows the subpulse, where the gray line corresponds to the subpulse data, the black line is the fit to the data, the red line is the envelope for a given bandwidth and the blue line is the microstructure signal defined as the difference between the red and black lines. The second panel correspond to the ACF of the microstructure (blue) signal. The timescales that we measure are indicated in the figure. The three sets of plots from top to bottom are for three different bandwidth values 0.1, 0.075 and 0.05, respectively (see text for details).
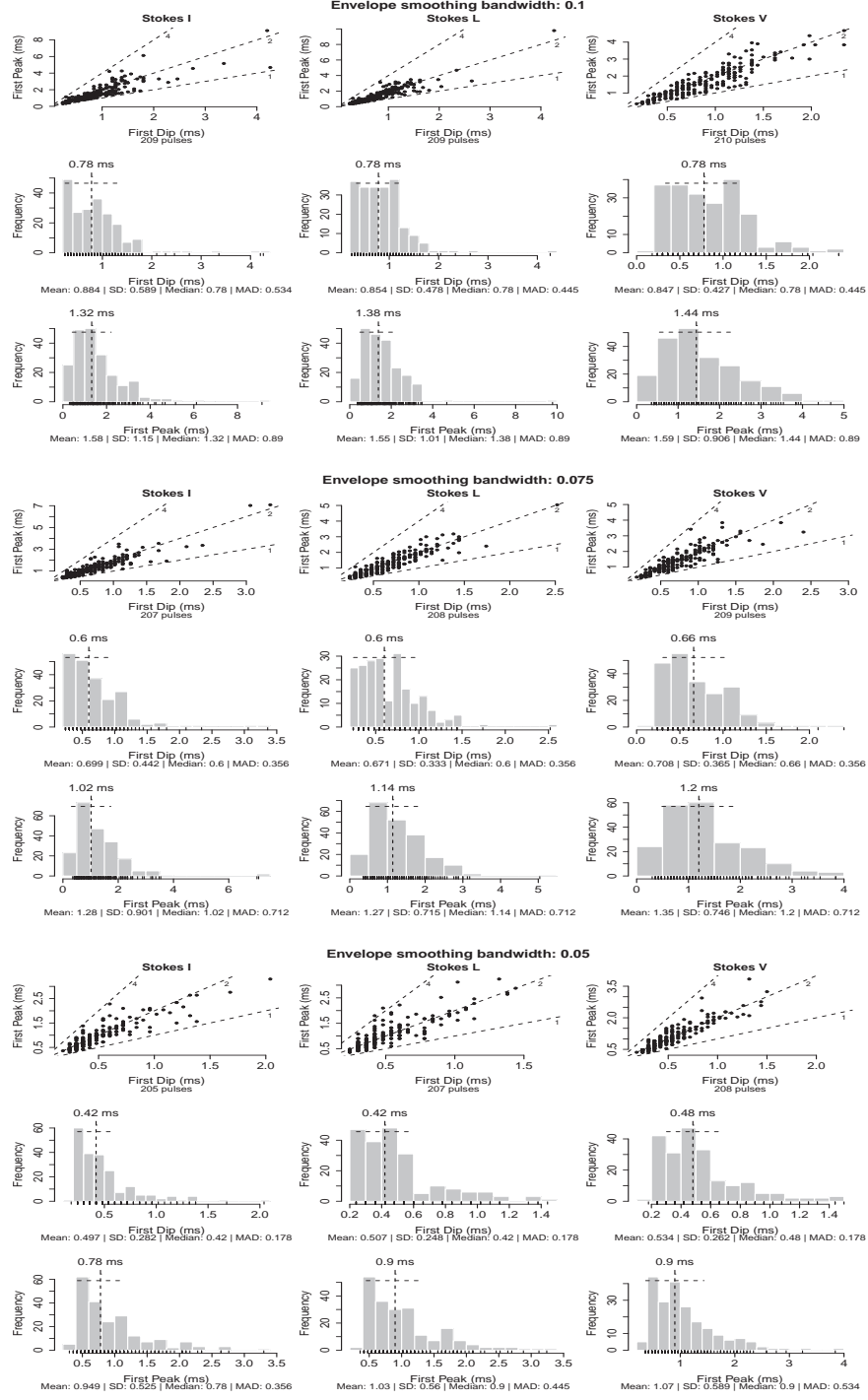
Fig. 6.— The three plots above are histograms of the estimated timescales of the microstructure signal for the trailing component of PSR B1133+16. The three sets of plots correspond to three different bandwidths $h = 0.1, 0.075$ and 0.05, respectively, from top to bottom . In each plot there are three columns corresponding to Stokes I, L & V from left to right, respectively. The topmost panel in each plot is the relation between the first dip (as x-axis) and first peak (as y-axis) of the ACF. The middle panel shows distribution of the first dip in the ACF which corresponds to t_μ. The bottom panel shows the distribution of the first peak in the ACF which correspond to P_μ (see text for details).
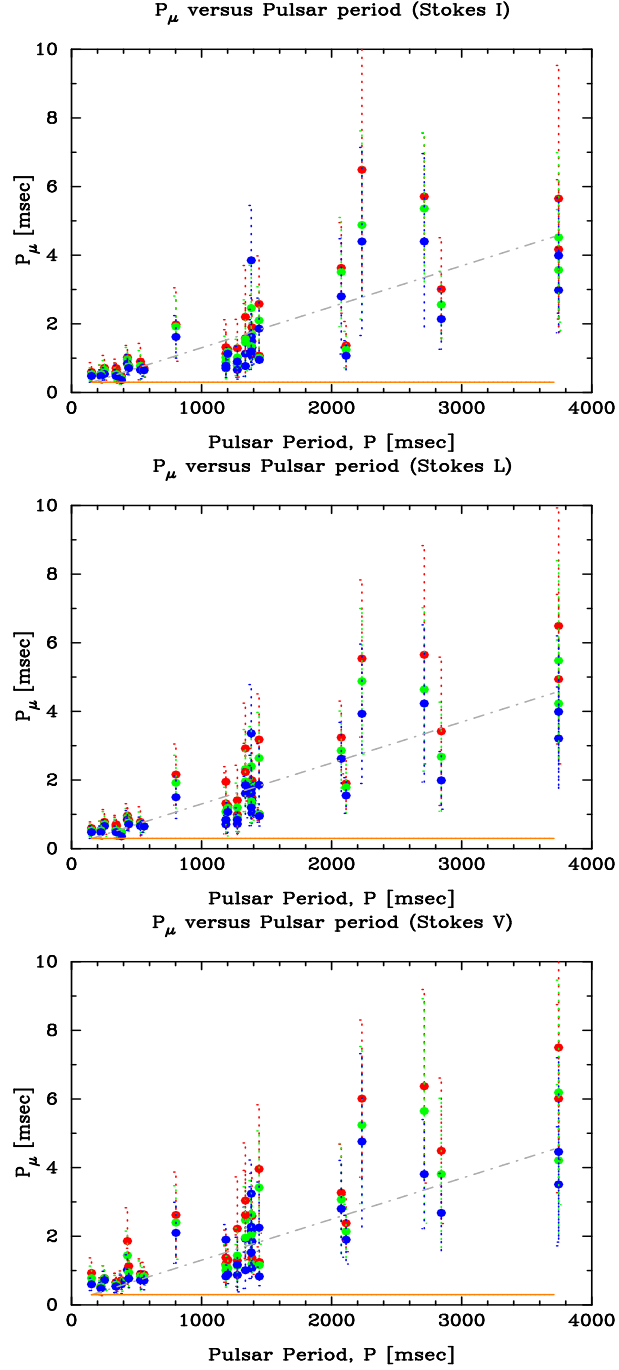
Fig. 7.— The median value of P_μ for all the pulsars as a function of pulsar period P is shown in the above plots. The three plots from top to bottom correspond to Stokes I, L and V, respectively. The red, green and blue points corresponds to bandwidths of 0.1, 0.075 and 0.05, respectively. The dashed line is a fit to the median P_μ values. The orange line at 300 μsec along the abscissa is about five times the time resolution of our observations.
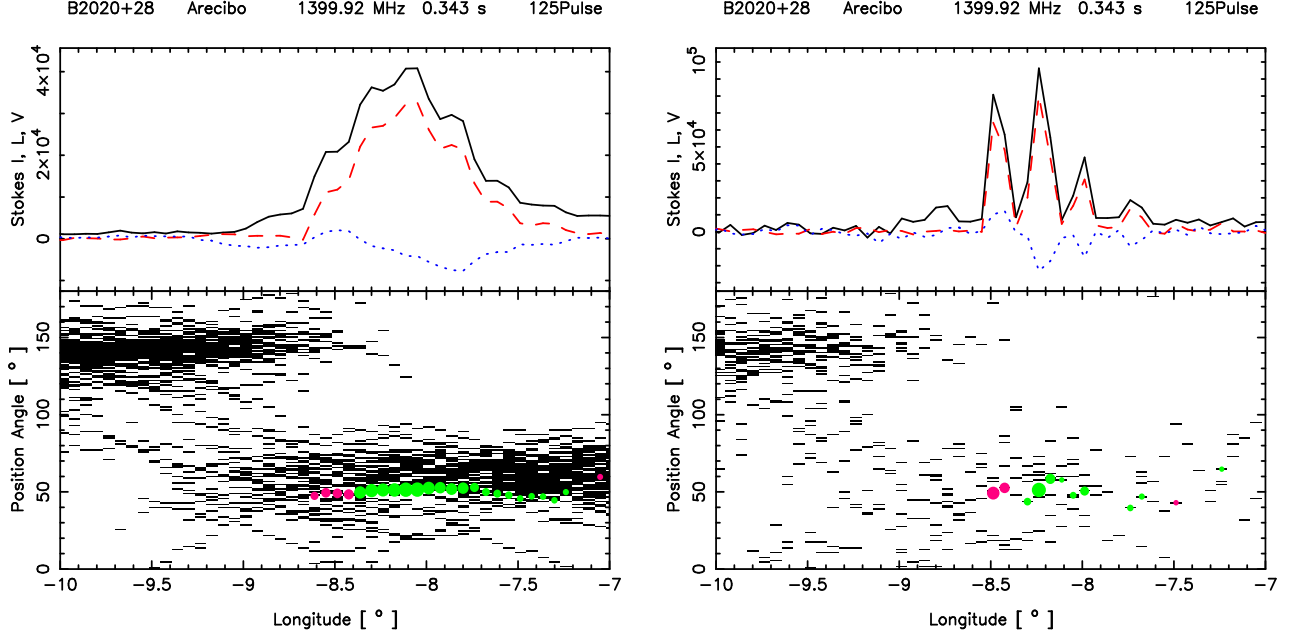
Fig. 8.— The left plot shows a subpulse of PSR B2020+28 as in Fig. 1, which has been smoothed to time resolution of 595.2 μsec. Note that the subpulse is close to 100% linearly polarized and shows a sign-changing circular. The corresponding right display shows the high resolution pulse with time resolution 59.52μsec. The striking point to note there is that the subpulse is split into microstructures, with the linear and circular polarization following the same width and periodicity as that of the total intensity. These microstructures hence do not represent coherent curvature radiation by charged bunches in vaccum (see text for details).
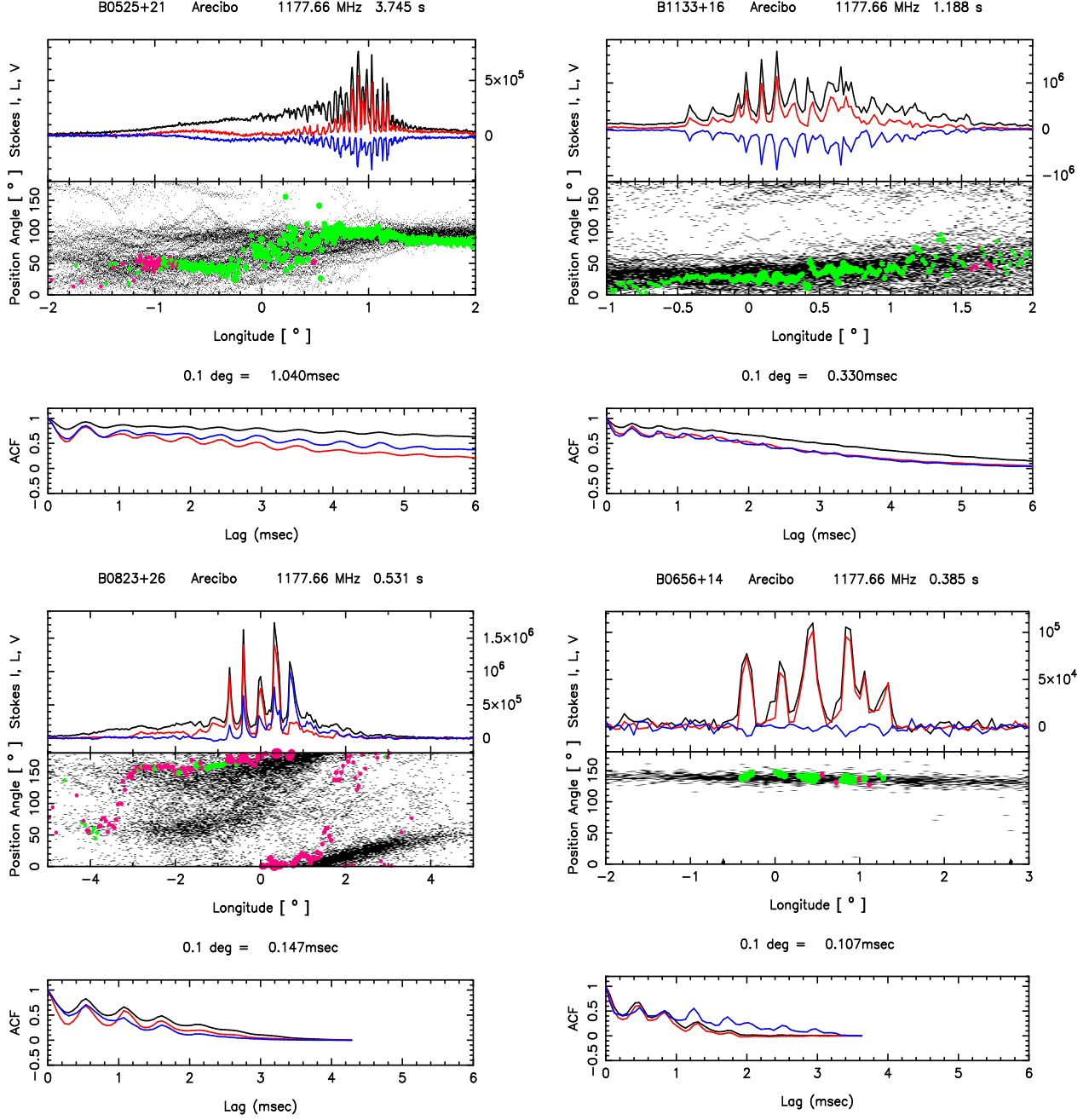
Fig. 9.— A few archetypal examples (as in Fig. 1) illustrating that the circular polarization follows the same P_μ values as the total intensity and linear polarization. In each display a highly resolved subpulse is shown, and in the bottom panel the ACF of the Stokes parameters are shown. Note that in all the examples the PPA across the subpulse is primarily associated with a single polarization mode. Clearly the ACFs of Stokes I, L and V trace each other extremely well.

Table 1.   Observational Parameters: Column 1 to 4 in the table below lists the pulsar name, observatory, observing frequency and the observing MJD. Column 5 gives the Channel bandwidth and the total number of channels across the band. Column 6 gives the total number of pulses observed/resolution in degrees/resolution in μsec. Column 7 and 8 gives the pulsar period and the dispersion measure (DM)used for our analysis. Note that Pulsar name with boldfaces are the ones used for microstructure timescale estimate analysis.

PSR Name	Band (MHz)	MJD	Ch.BW (GHz)/ Nchan	length res ($^\circ$)/μsec	Per sec	DM pc/cc
B0301+19	326.9	55283	0.085/256	616/0.015/59.52	1.387	15.74
B0525+21	326.9	56572	0.085/256	616/0.015/59.52	3.745	50.94
J0546+2441	327.18	56573	0.024/1024	843/0.021/166.67	2.843	73.81
B1919+21	324.1	55320	0.112/512	1139/0.016/62.5	1.337	12.46
B1929+10	326.9	55320	0.085/256	4639/0.094/59.52	0.226	3.18
B1944+17	324.1	55320	0.112/512	2269/0.051/62.5	0.440	16.22
B2016+28	326.9	55320	0.085/256	953/0.038/59.52	0.557	14.17
B2020+28	326.9	55320	0.085/256	4211/0.062/59.52	0.343	24.64
B2044+15	326.9	55320	0.085/256	960/0.019/59.52	1.138	39.84
B2110+27	326.9	55320	0.085/256	1265/0.018/59.52	1.202	25.11
B2315+21	324.1	55275	0.112/512	275/0.015/59.52	1.444	20.91
B0301+19	1177.6	55425	0.085/1024	1202/0.015/59.52	1.387	15.74
J0546+2441	1178.0	56572	0.085/1024	421/0.007/59.52	2.843	73.81
B0525+21	1177.6	55522	0.085/1024	640/0.006/59.52	3.745	50.94
B0656+14	1177.6	55522	0.085/1024	1558/0.055/59.52	0.384	13.997
B0751+32	1177.6	55522	0.085/1024	1944/0.014/59.52	1.442	39.949
B0823+26	1177.6	55522	0.085/1024	1130/0.040/59.52	0.530	19.454
B0834+06	1177.6	55522	0.085/1024	1006/0.017/59.52	1.274	12.889
B0919+06	1177.6	55522	0.085/1024	1045/0.049/59.52	0.430	27.271
B0950+08	1177.6	55522	0.085/1024	2055/0.084/59.52	0.253	2.958
B1133+16	1177.6	55522	0.085/1024	2104/0.018/59.52	1.187	4.864
B1237+25	1177.6	56550	0.085/1024	873/0.015/59.52	1.382	9.242
J1503+2111	1177.4	56550	0.085/1024	1025/0.006/59.52	3.314	11.75
B1534+12	1212.3	55637	0.067/512	15835/0.36/38.69	0.037	11.614
J1713+0747	1177.6	55632	0.085/1024	65646/4.735/59.52	0.005	15.9915
B1737+13	1177.6	55632	0.085/1024	747/0.026/59.52	0.803	48.673
J1720+2150	1178.0	56550	0.086/1024	1021/0.013/59.52	1.615	41.4
J1740+1000	1177.6	55632	0.085/1024	3893/0.139/59.52	0.154	23.85
J1746+2245	1178.0	56550	0.085/1024	899/0.006/59.52	3.465	52.0

Table 1—Continued

PSR Name	Band (MHz)	MJD	Ch.BW (GHz)/ Nchan	length res (°)/μsec	Per sec	DM pc/cc
B1855+09	1177.7	55637	0.086/1024	111910/4./59.52	0.005	13.295
B1901+10	1177.7	56563	0.085/1024	1034/0.011/59.52	1.856	135
B1910+20	1177.7	56563	0.085/1024	1025/0.009/59.52	2.233	88.34
J1910+0714	1177.7	56563	0.085/1024	1024/0.007/59.52	2.712	124.06
B1919+21	1433.9	56207	0.672/128	346/0.016/59.52	1.337	12.46
B1929+10	1177.6	55633	0.085/1024	2648/0.095/59.52	0.226	3.180
B1944+17	1177.6	55633	0.085/1024	1361/0.048/59.52	0.440	16.22
B2002+31	1177.6	56564	0.085/1024	1054/0.010/59.52	2.111	234.82
B2016+28	1177.6	55632	0.085/1024	1075/0.038/59.52	0.557	14.172
B2020+28	1177.6	55632	0.085/1024	1747/0.062/59.52	0.343	24.64
B2034+19	1178.1	56564	0.085/1024	1341/0.014/59.52	2.074	36.0
B2110+27	1177.6	55425	0.085/1024	1625/0.018/59.52	1.202	25.113
B2113+14	1177.6	55425	0.085/1024	1060/0.048/59.52	0.440	56.149
B2315+21	1177.6	55425	0.085/1024	746/0.014/59.52	1.444	20.906

Table 2.   The median P_μ values for mircrostructures for all the Stokes parameters. In column 2 the longitude range is the window that has been used for analysis and this region of the pulse can be seen in the average profiles given in the appendix. In column 5, 6 and 7 the median P_μ value is given and the values in the parenthesis correspond to the median absolute deviation of the P_μ values. Column 9 gives the value of the bandwidth h used for analysis and column 10 gives the number of points in the pulse window (see text for further details).

| | | | | Median P_μ from ACF histogram | | | | |
PSR Bname	Longitude Range (°)	Freq. (GHz)	Period (sec)	$\overline{P_\mu^I}$ (msec)	P_μ^L (msec)	P_μ^V (msec)	h	NPT
B0301+19	-2.2 — 2.5	1.1	1.387	1.49 (0.53)	1.49 (0.62)	1.37 (0.48)	0.10	301
B0301+19		1.1	1.387	1.19 (0.44)	1.31 (0.48)	1.19 (0.35)	0.075	301
B0301+19		1.1	1.387	1.07 (0.27)	1.04 (0.31)	1.07 (0.35)	0.05	301
B0301+19	-11.8 — -5.2	1.1	1.387	1.90 (0.93)	1.99 (0.93)	2.59 (1.24)	0.10	427
B0301+19		1.1	1.387	1.70 (0.71)	1.85 (0.79)	2.11 (0.91)	0.075	427
B0301+19		1.1	1.387	1.31 (0.48)	1.40 (0.48)	1.85 (0.88)	0.05	427
J0546+2441	-2.13 — 1.81	1.1	2.843	3.01 (1.5)	3.42 (2.16)	4.49 (2.12)	0.10	504
J0546+2441		1.1	2.843	2.56 (0.97)	2.68 (1.59)	3.81 (2.21)	0.075	504
J0546+2441		1.1	2.843	2.14 (0.88)	1.99 (0.84)	2.68 (1.15)	0.050	504
B0525+21	-2.85 — 2.86	1.1	3.745	4.17 (2.03)	4.94 (2.47)	6.01 (2.74)	0.10	1001
B0525+21		1.1	3.745	3.57 (1.76)	4.23 (1.85)	4.21 (2.21)	0.075	1001
B0525+21		1.1	3.745	2.98 (1.24)	3.21 (1.50)	3.51 (1.68)	0.050	1001
B0525+21	-14.3 — -10.9	1.1	3.745	5.65 (3.88)	6.49 (3.44)	7.50 (3.27)	0.10	1201
B0525+21		1.1	3.745	4.52 (2.47)	5.48 (2.91)	6.19 (3.27)	0.075	1201
B0525+21		1.1	3.745	3.99 (1.68)	3.99 (2.21)	4.46 (2.74)	0.050	1201
B0656+14	-0.61 — 4.95	1.1	0.384	0.48 (0.18)	0.48 (0.18)	0.72 (0.27)	0.10	101
B0656+14		1.1	0.384	0.42 (0.18)	0.48 (0.18)	0.66 (0.26)	0.075	101
B0656+14		1.1	0.384	0.36 (0.09)	0.36 (0.09)	0.60 (0.27)	0.05	101
B0751+32	-2.24 — 2.43	1.1	1.442	2.58 (1.4)	3.18 (1.33)	3.96 (1.87)	0.10	304
B0751+32		1.1	1.442	2.10 (0.98)	2.64 (1.33)	3.42 (1.65)	0.075	304
B0751+32		1.1	1.442	1.86 (0.89)	1.86 (1.20)	2.25 (1.33)	0.050	304
B0823+26	-1.65 — 1.41	1.1	0.530	0.90 (0.53)	0.78 (0.44)	0.90 (0.44)	0.10	264
B0823+26		1.1	0.530	0.78 (0.44)	0.72 (0.35)	0.84 (0.44)	0.075	264
B0823+26		1.1	0.530	0.66 (0.26)	0.66 (0.26)	0.72 (0.26)	0.050	264

Table 2—Continued

PSR Bname	Longitude Range (°)	Freq. (GHz)	Period (sec)	Median P_μ from ACF histogram			h	NPT
				P_μ^I (msec)	P_μ^L (msec)	P_μ^V (msec)		
B0834+06	-1.32 — 1.46	1.1	1.275	0.84 (0.40)	0.99 (0.49)	1.29 (0.75)	0.10	167
B0834+06		1.1	1.275	0.78 (0.27)	0.90 (0.40)	1.14 (0.62)	0.075	167
B0834+06		1.1	1.275	0.66 (0.27)	0.72 (0.27)	0.87 (0.49)	0.050	167
B0834+06	3.7 — 7.2	1.1	1.275	1.29 (0.84)	1.41 (1.02)	2.22 (1.51)	0.10	210
B0834+06		1.1	1.275	1.02 (0.53)	1.20 (0.71)	1.44 (0.80)	0.075	210
B0834+06		1.1	1.275	0.90 (0.44)	0.84 (0.35)	1.17 (0.80)	0.050	210
B0919+06	-7.5 — 4.74	1.1	0.430	1.02 (0.35)	0.96 (0.35)	1.86 (0.97)	0.10	249
B0919+06		1.1	0.430	0.96 (0.35)	0.90 (0.27)	1.44 (0.71)	0.075	249
B0919+06		1.1	0.430	0.84 (0.27)	0.84 (0.27)	1.02 (0.44)	0.050	249
B0950+08	-12.77 — 10.84	1.1	0.253	0.72 (0.36)	0.78 (0.36)	0.78 (0.36)	0.10	279
B0950+08		1.1	0.253	0.66 (0.27)	0.72 (0.36)	0.78 (0.36)	0.075	279
B0950+08		1.1	0.253	0.54 (0.18)	0.66 (0.18)	0.72 (0.26)	0.050	279
B1133+16	-1.47 — 3.39	1.1	1.187	1.13 (0.70)	1.95 (0.44)	1.19 (0.53)	0.10	271
B1133+16		1.1	1.187	0.89 (0.44)	0.83 (0.35)	1.01 (0.44)	0.075	271
B1133+16		1.1	1.187	0.71 (0.27)	0.71 (0.26)	0.83 (0.35)	0.050	271
B1133+16	3.39 — 8.8	1.1	1.187	1.32 (0.80)	1.32 (0.89)	1.38 (0.80)	0.10	301
B1133+16		1.1	1.187	1.02 (0.62)	1.08 (0.71)	1.14 (0.62)	0.075	301
B1133+16		1.1	1.187	0.78 (0.35)	0.84 (0.36)	1.90 (0.44)	0.050	301
B1237+25	-2.07 — 4.3	1.1	1.382	3.85 (1.60)	3.36 (1.42)	3.24 (0.98)	0.01	401
B1237+25		1.1	1.382	2.46 (1.25)	2.40 (1.16)	2.64 (0.98)	0.075	401
B1237+25		1.1	1.382	1.62 (0.80)	1.62 (0.80)	2.28 (1.16)	0.050	401
B1237+25	8.77 — 11.87	1.1	1.382	1.50 (0.62)	1.74 (0.98)	2.16 (1.07)	0.01	201
B1237+25		1.1	1.382	1.35 (0.67)	1.38 (0.62)	2.04 (1.07)	0.075	201

Table 2—Continued

PSR Bname	Longitude Range (°)	Freq. (GHz)	Period (sec)	Median P_μ from ACF histogram			h	NPT
				P_μ^I (msec)	P_μ^L (msec)	P_μ^V (msec)		
B1237+25		1.1	1.382	1.20 (0.53)	1.20 (0.53)	1.53 (0.76)	0.050	201
B1737+13	-7.94 — 5.41	1.1	0.803	1.98 (1.07)	2.16 (0.89)	2.62 (1.25)	0.10	501
B1737+13		1.1	0.803	1.92 (0.89)	1.92 (0.80)	2.40 (1.07)	0.075	501
B1737+13		1.1	0.803	1.62 (0.62)	1.50 (0.62)	2.10 (0.89)	0.050	501
J1740+1000	-4.87 — 10.7	1.1	0.154	0.60 (0.27)	0.60 (0.18)	0.93 (0.44)	0.10	113
J1740+1000		1.1	0.154	0.54 (0.18)	0.54 (0.18)	0.78 (0.35)	0.075	113
J1740+1000		1.1	0.154	0.48 (0.18)	0.48 (0.18)	0.60 (0.18)	0.050	113
B1910+20	-1.21 — 6.46	1.1	2.233	6.49 (3.53)	5.54 (2.29)	6.01 (2.29)	0.10	801
B1910+20		1.1	2.233	4.88 (2.74)	4.88 (2.12)	5.24 (2.29)	0.075	801
B1910+20		1.1	2.233	4.40 (2.74)	3.93 (2.03)	4.76 (2.56)	0.050	801
J1910+0714	-1.41 — 3.91	1.1	2.712	5.71 (1.85)	5.65 (3.18)	6.37 (2.82)	0.10	675
J1910+0714		1.1	2.712	5.36 (2.21)	4.64 (2.38)	5.65 (3.27)	0.075	675
J1910+0714		1.1	2.712	4.40 (2.56)	4.23 (2.29)	3.81 (1.59)	0.050	675
B1919+21	-2.45 — 3.10	1.1	1.337	1.58 (1.01)	2.92 (1.32)	3.04 (1.68)	0.10	348
B1919+21		1.1	1.337	1.46 (0.83)	2.32 (1.15)	2.47 (0.97)	0.075	348
B1919+21		1.1	1.337	1.13 (0.35)	1.61 (0.71)	1.93 (0.92)	0.050	348
B1919+21	5.28 — 8.48	1.1	1.337	2.20 (1.50)	2.23 (0.84)	2.62 (1.30)	0.10	201
B1919+21		1.1	1.337	1.55 (1.15)	1.96 (0.88)	1.96 (0.88)	0.075	201
B1919+21		1.1	1.337	0.77 (0.26)	1.85 (0.26)	1.01 (0.53)	0.050	201
B1929+10	-11.1 — 7.84	1.1	0.226	0.54 (0.26)	0.54 (0.26)	0.53 (0.26)	0.10	201
B1929+10		1.1	0.226	0.54 (0.26)	0.54 (0.26)	0.54 (0.18)	0.075	201
B1929+10		1.1	0.226	0.48 (0.18)	0.48 (0.18)	0.48 (0.18)	0.050	201
B1944+17	-9.67 — 4.91	1.1	0.440	0.77 (0.27)	0.83 (0.35)	1.13 (0.52)	0.10	301

Table 2—Continued

PSR Bname	Longitude Range (°)	Freq. (GHz)	Period (sec)	Median P_μ from ACF histogram			h	NPT
				P_μ^I (msec)	P_μ^L (msec)	P_μ^V (msec)		
B1944+17		1.1	0.440	0.77 (0.27)	0.77 (0.27)	0.95 (0.44)	0.075	301
B1944+17		1.1	0.440	0.71 (0.18)	0.71 (0.18)	0.77 (0.27)	0.050	301
B2002+31	-2.48 — 2.01	1.1	2.111	1.37 (0.70)	1.90 (0.79)	2.38 (0.83)	0.10	445
B2002+31		1.1	2.111	1.25 (0.53)	1.79 (0.79)	2.14 (0.79)	0.075	445
B2002+31		1.1	2.111	1.07 (0.44)	1.55 (0.52)	1.90 (0.71)	0.050	445
B2016+28	-5.34 — 4.45	1.1	0.557	0.71 (0.26)	0.65 (0.17)	0.89 (0.35)	0.10	256
B2016+28		1.1	0.557	0.65 (0.18)	0.65 (0.18)	0.83 (0.26)	0.075	256
B2016+28		1.1	0.557	0.65 (0.17)	0.65 (0.17)	0.71 (0.27)	0.050	256
B2020+28	-11.27 — -5.03	1.1	0.343	0.71 (0.26)	0.71 (0.26)	0.66 (0.26)	0.10	101
B2020+28		1.1	0.343	0.60 (0.26)	0.60 (0.26)	0.54 (0.18)	0.075	101
B2020+28		1.1	0.343	0.54 (0.26)	0.54 (0.26)	0.54 (0.18)	0.050	101
B2020+28	-3.78 — 1.21	1.1	0.343	0.60 (0.26)	0.66 (0.26)	0.66 (0.26)	0.10	98
B2020+28		1.1	0.343	0.54 (0.18)	0.54 (0.26)	0.60 (0.26)	0.075	98
B2020+28		1.1	0.343	0.48 (0.18)	0.48 (0.18)	0.54 (0.18)	0.050	98
B2034+19	-5.25 — -1.49	1.1	2.074	3.63 (1.32)	3.24 (1.06)	3.27 (1.41)	0.10	361
B2034+19		1.1	2.074	3.51 (1.59)	2.86 (1.15)	3.07 (1.63)	0.075	361
B2034+19		1.1	2.074	2.80 (1.68)	2.62 (1.06)	2.80 (1.41)	0.050	361
B2110+27	-1.3 — 2.26	1.1	1.202	1.25 (0.09)	1.25 (0.09)	1.31 (0.44)	0.10	201
B2110+27		1.1	1.202	1.19 (0.09)	1.19 (0.18)	1.07 (0.35)	0.075	201
B2110+27		1.1	1.202	1.13 (0.18)	1.07 (0.27)	0.89 (0.27)	0.050	201
B2315+21	-1.79 — 1.17	1.1	1.444	1.07 (0.09)	1.01 (0.18)	1.25 (0.44)	0.10	201
B2315+21		1.1	1.444	1.01 (0.09)	1.01 (0.09)	1.16 (0.40)	0.075	201
B2315+21		1.1	1.444	0.95 (0.09)	0.95 (0.18)	0.83 (0.27)	0.050	201

A. Methods

A.1. Models for data and noise

The measured signal Y_i at time t_i is modeled as

$$Y_i = f(t_i) + \epsilon_i, \tag{A1}$$

where f embodies the true but unknown variation of the subpulse signal with time, and ϵ_i represents the noise in the data. The N time points t_i where signal is measured are assumed to be equidistant; *i.e.,* of the form $t_i = i\delta$ where $i = 0, 1, \ldots, N - 1$. ($\delta = 59.5\mu$s is the time resolution for all the data sets analyzed in this work). Without loss of generality, we take $\delta = 1$ (which amounts to redefining the time unit). The noise variables ϵ_i are assumed to be independent with mean 0 and a (constant) variance σ^2. Our present analysis does not require an estimate of the noise variance explicitly (except for the purpose of choosing high-S/N pulses; see Sec. 3). We have modeled the true signal f underlying the subpulse data as

$$f(t) = e(t) + m(t), \tag{A2}$$

where e and m respectively represent a smooth slow-varying envelope and faster-scale quasiperiodic modulations corresponding to microstructure. The methodology in Sec. A.3 is used to estimate f optimally, whereas e is estimated using the method in Sec. A.4. The difference $f(t) - e(t)$ is taken to be the estimated microstructure. Fig. 4 shows examples of such fit-envelope-microstructure decomposition for a few subpulses. The model A1 is inspired by the observation based on Fig. 4 that the ACF is dominated by the envelope feature which should be removed from the data to extract the microstructure.

A.2. Outliers

Radio-frequency interference (RFI) over timescales that are much smaller than the pulse period may introduce isolated outliers in the subpulse time series which may have detrimental effect on the downstream analysis. For example, outliers may cause fluctuations in the fit that may have an effect on the ACF used for timescale identification. Therefore, before engaging into any further analysis, we first assess the extent of contamination in a data set (through visual inspection of subpulses) and, if deemed necessary, we identify (and "curate") potential outliers in all the subpulse time series in the data set heuristically as explained below. In this work, we have used the heuristic approach described below because of its simplicity. We note, however, that better alternatives to our heuristic approach could be the use of robust nonparametric regression methods (Härdle 1992; Efromovich 1999) that deal with outliers in the regression context in a unified manner, or outlier identification methods with established formal properties.

Fig. A1 shows examples of subpulses (#42, #44, #45) with clear outliers from a PSR B0525+21 data set. In fact, this was the only data set in the present study which showed clear outliers.

Further, for this data set, it was known that these outliers were caused by radio communication from a satellite in the field of view. Fig. A1 also shows a subpulse (#298) from the same data set which illustrates a failure of our heuristic method for outlier identification. This subpulse has strong and highly ringing microstructure which results into too many data points in the ringing part being wrongly tagged as potential outliers. Since we expect at most a few isolated outliers in any subpulse (say, less than 1% of the subpulse length), such over-identification can be easily detected. Outlier correction, as described below, is not applied to such subpulses.

Identifying potential outliers.   When the data contain an unknown trend f, it is necessary to identify a potential outlier with respect to data values in its local neighbourhood. Therefore, we first obtain a pilot fit $\widehat{f}_o$ through kernel regression (Wasserman 2006; Härdle 1992). The smoothing bandwidth for this pilot fit may be taken as a constant b times the optimal smoothing bandwidth obtained via cross-validation; slight oversmoothing ($b > 1$) is expected to help make the fit $\widehat{f}_o$ somewhat robust against outliers. Any data point i with a relatively large residual $r_i = Y_i - \widehat{f}_o(t_i)$ is a potential outlier: Specifically, following the standard prescription (Frigge et al. 1989), the ith data point is tagged as a potential outlier if $r_i > r_{75} + a \times (r_{75} - r_{25})$ or $r_i < r_{25} - a \times (r_{75} - r_{25})$, where r_{75} and r_{25} are respectively the 75 and 25 percentile points for the residual vector ($r_{75} - r_{25}$ is therefore the interquartile range). The value of the multiplier a is taken to be 3 instead of the conventional 1.5 to make outlier identification more conservative.

Imputing potential outliers back into data.   We replace a potential isolated outlier value Y_i by the median of signal values in a small local neighbourhood of t_i. In this work, we have taken the size of the local neighbourhood to be 5 points on either side of t_i. That is, we replace a potential outlier value Y_i with the median of $Y_{i-5}, Y_{i-4}, Y_{i-3}, Y_{i-2}, Y_{i-1}, Y_{i+1}, Y_{i+2}, Y_{i+3}, Y_{i+4}, Y_{i+5}$, with data boundaries handled by truncation.

A.3.   Model-independent fit to subpulse time series data

The immense variability in the pulse shapes suggests that the separation of probable signal from noise is best done using a nonparametric regression method that only makes mild assumptions about the true but unknown regression function without pre-specifying its mathematical form. In particular, we use smoothing spline regression (Green & Silverman 1994) which may be seen as a penalized least-squares method with a penalty on the roughness of the fit. Optimal value for the smoothing parameter is chosen using the standard method of (generalized) cross-validation. The smoothness of the resultant fit can be expressed in terms of *degrees of freedom* (DF). DF can be interpreted as the effective number of free parameters of the fit. Specifically, a fit with greater fluctuation has larger DF, while a smoother fit has smaller DF.
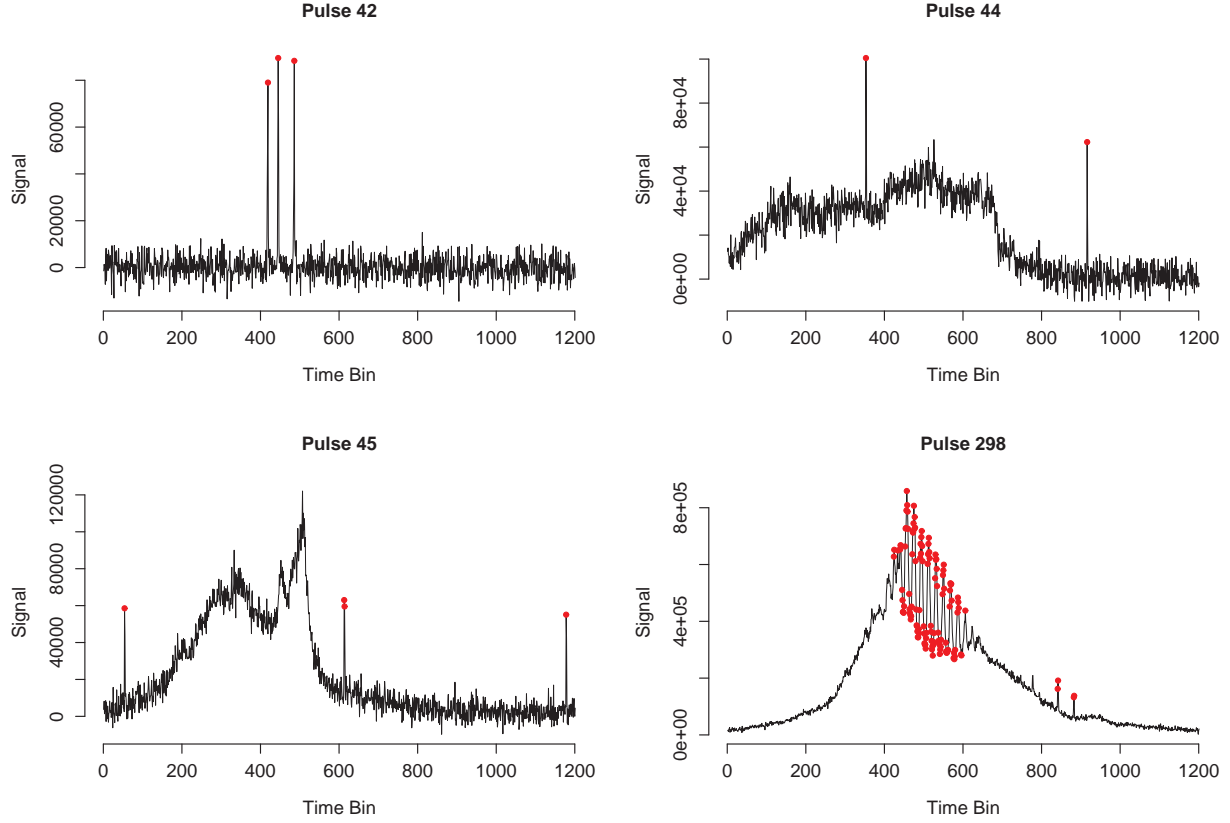
Fig. A1.— Subpulses 42, 44, 45, and 298 from a PSR B0525+21 data set illustrating the behaviour of our heuristic outlier identification method. See Sec. A.2 for description.

A.4. Estimating the pulse envelope

We use the Nadaraya-Watson kernel smoother (Wasserman 2006; Härdle 1992) to estimate the envelope of a subpulse by judiciously *oversmoothing* the data. Through trial-and-error, we found that the smoothing bandwidth $H \approx 0.075 \times N$ is more or less reasonable for all the pulsar data sets we analyzed. However, considering that the smoothing bandwidth for the envelope is perhaps the most critical parameter of our methodology, and that there does not appear to be any principled way of arriving at a prescription for it, we report results for a number of values of $h \equiv H/N$ over a plausible range; the rational for this range is discussed in Sec. 4.

A.5. Plots for average profiles

The average profiles and polarization position angle (PPA) histograms for all the pulsars given in Table. 1 are presented.
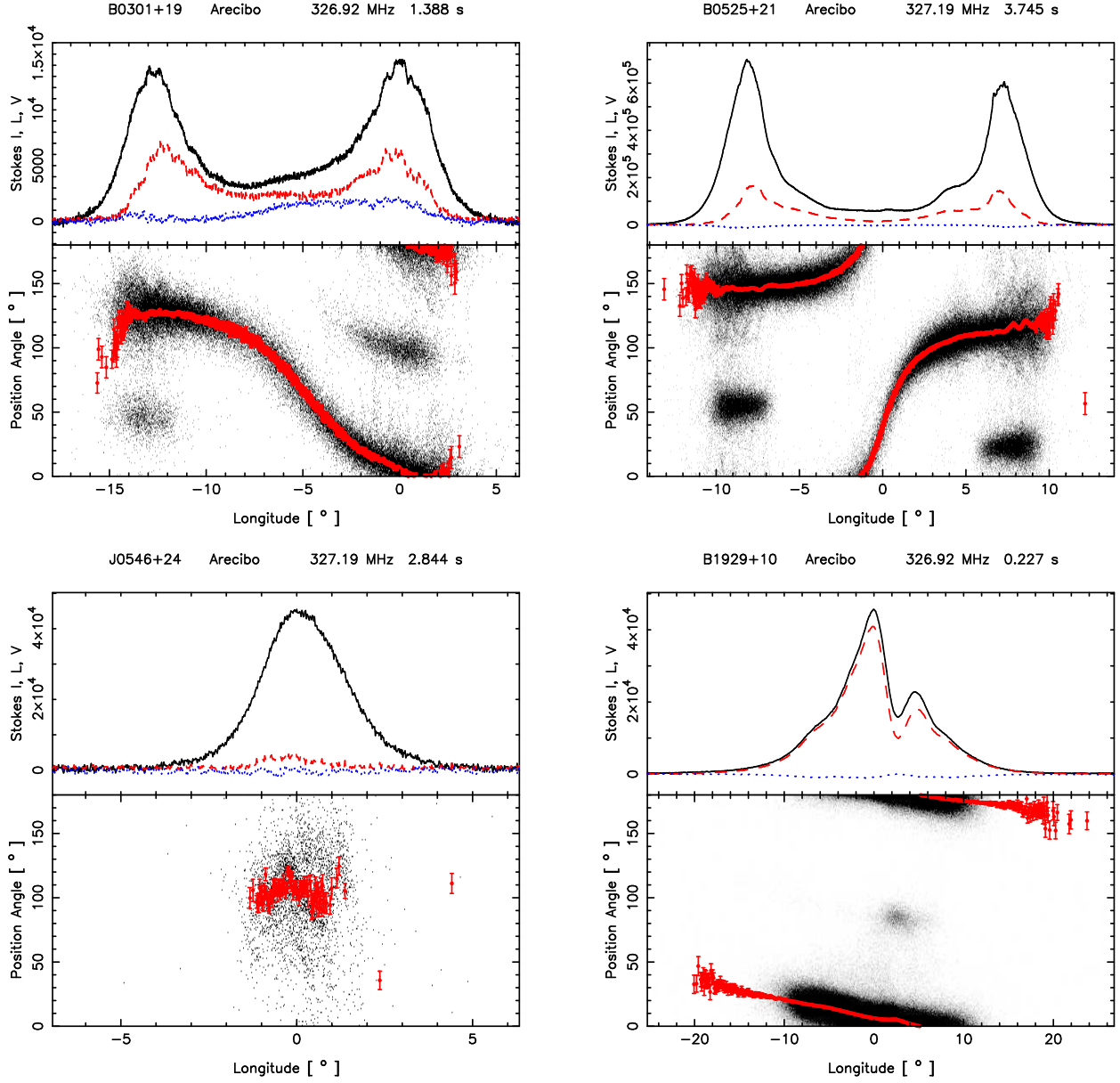
Fig. A2.— PPA histograms for pulsars PSR B0301+19, B0525+21, J0546+2441 and B1929+10 observed with time resolution of 59.5 μsec, where the instrument and band is indicated above each plot. The respective upper panels give the total power (black), total linear (red) and circular polarization LH-RH (blue). The lower panels give the polarization-angle density as black dots and the average PPA is plotted as red points.
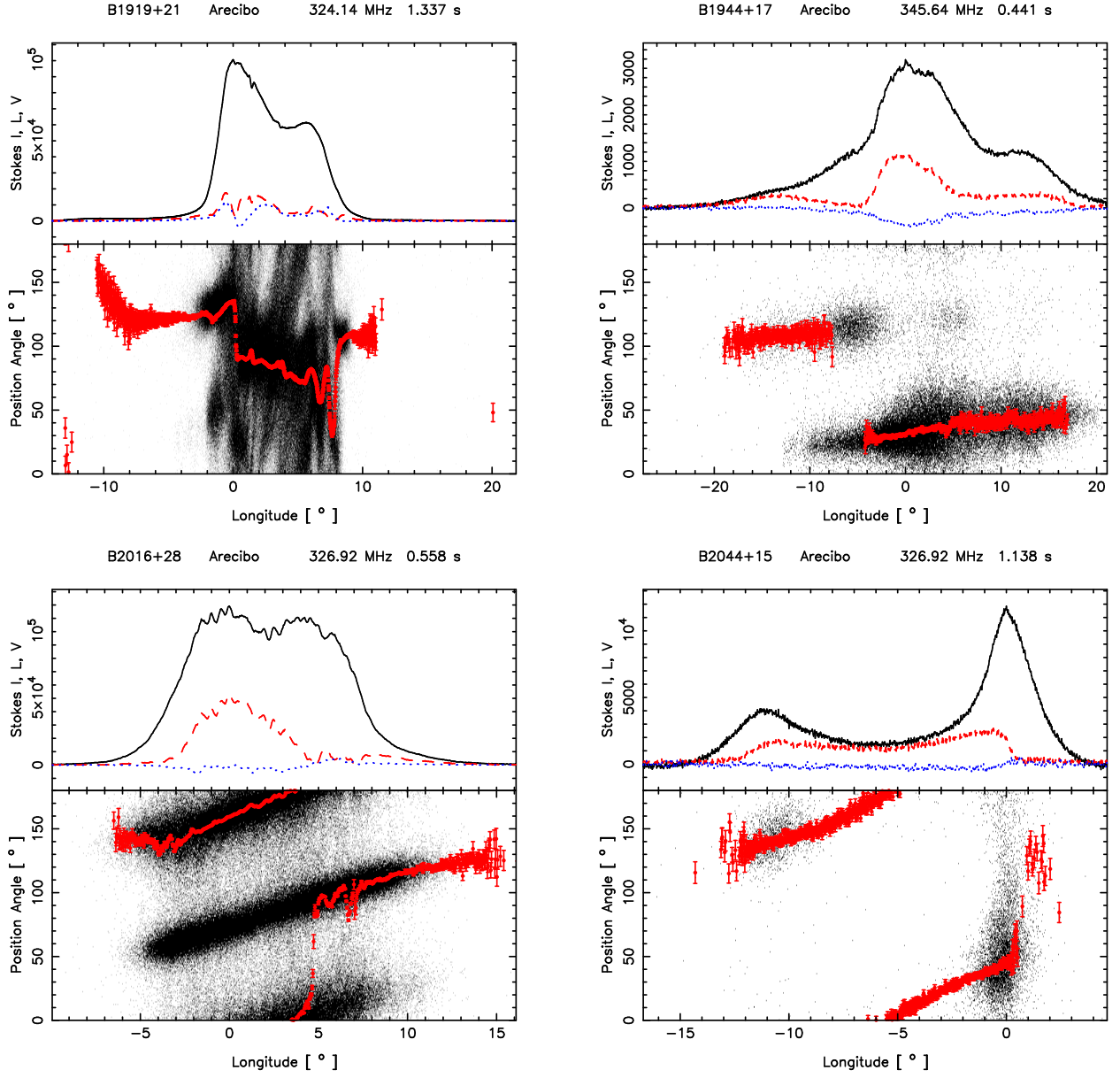
Fig. A3.— PPA histograms as in Fig. A2 for pulsars B1919+21, B1944+17, B2016+28 and B2044+15 observed with time resolutions of 59.5μsec.
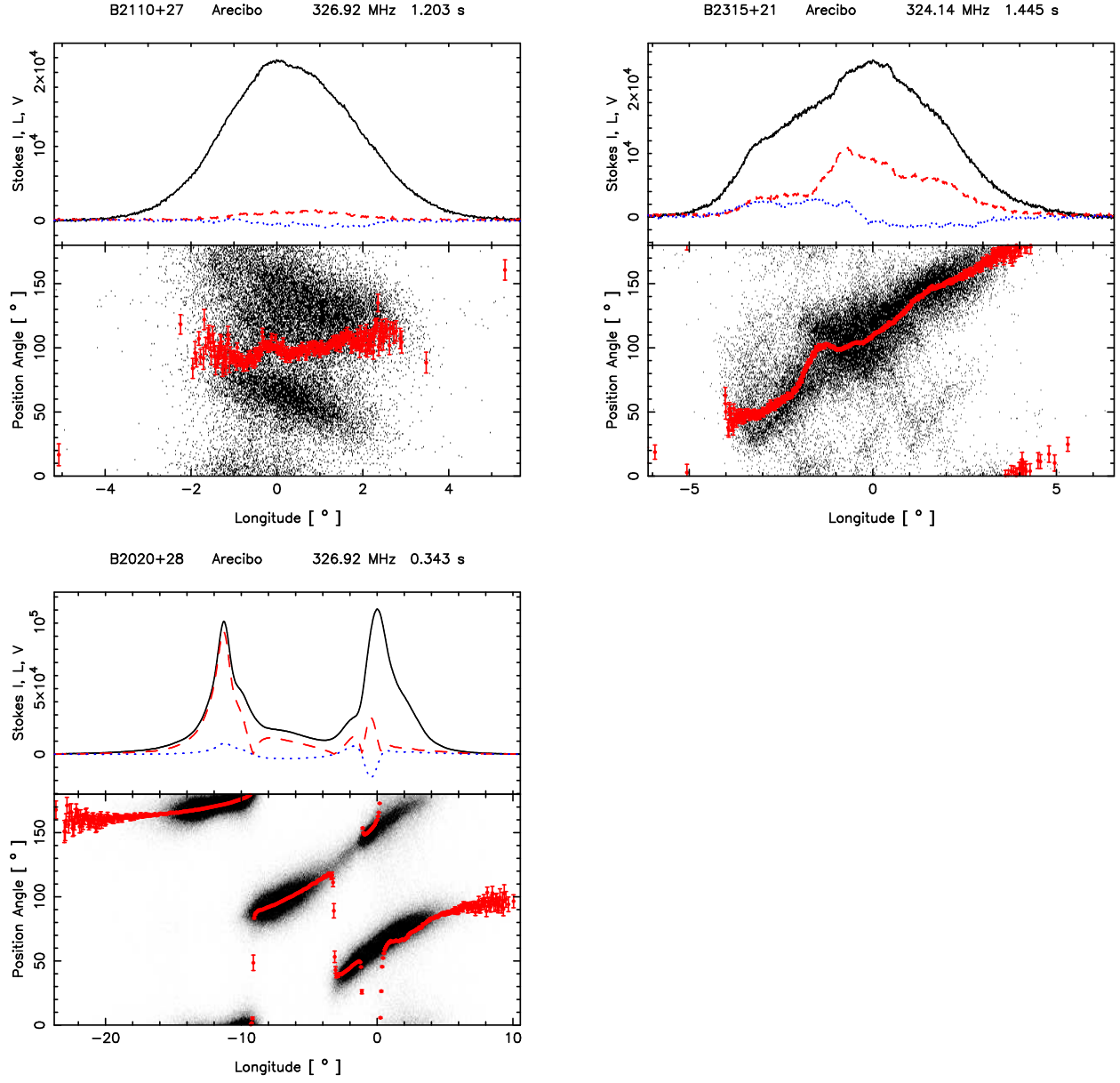
Fig. A4.— PPA histograms as in Fig. A2 for pulsars B2110+27, B2315+21 and B2020+28 observed with time resolutions of 59.5μsec.
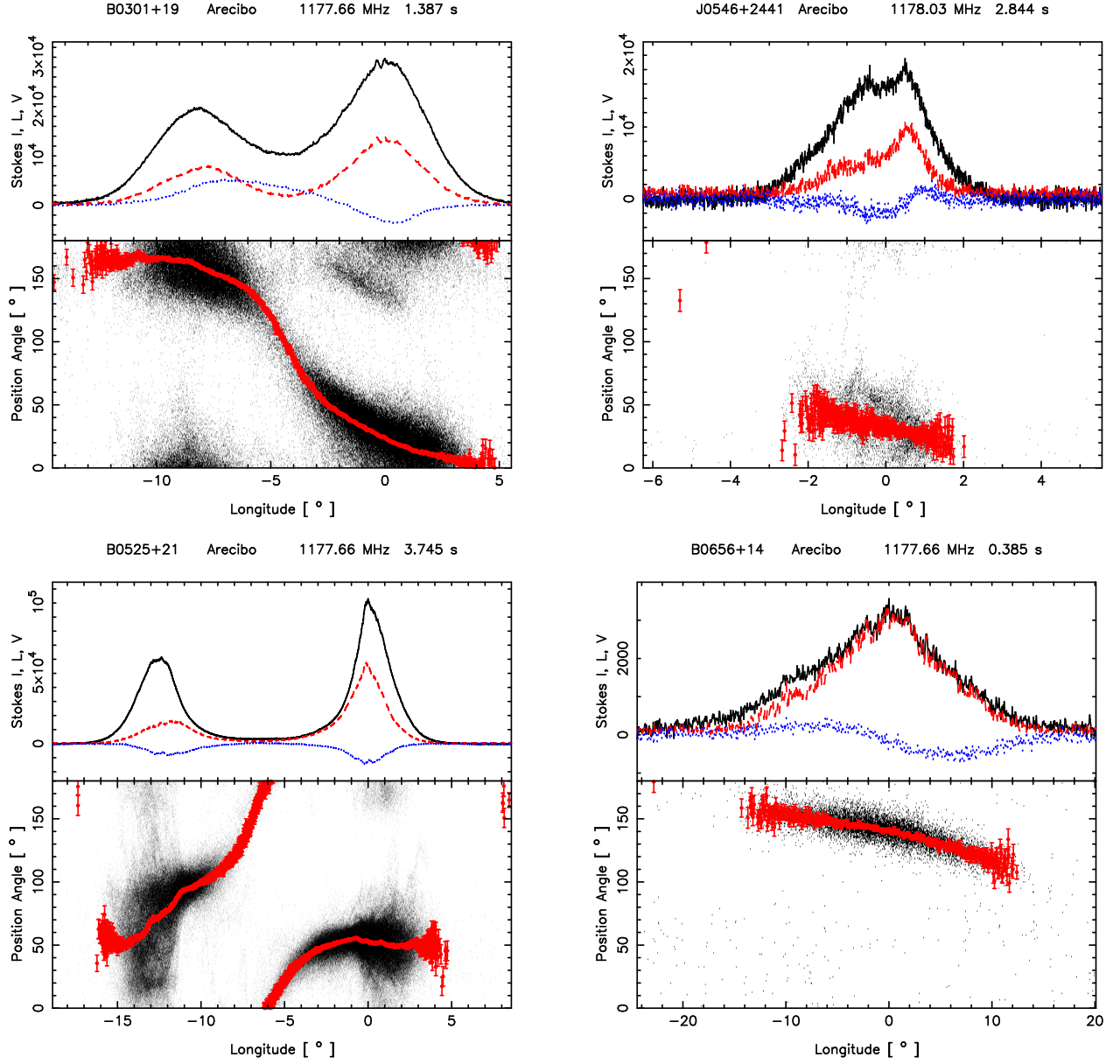
Fig. A5.— PPA histograms as in Fig. A2 for pulsars B0301+19, J0546+2441, B0525+21 and B0656+14 observed with time resolutions of 59.5μsec.
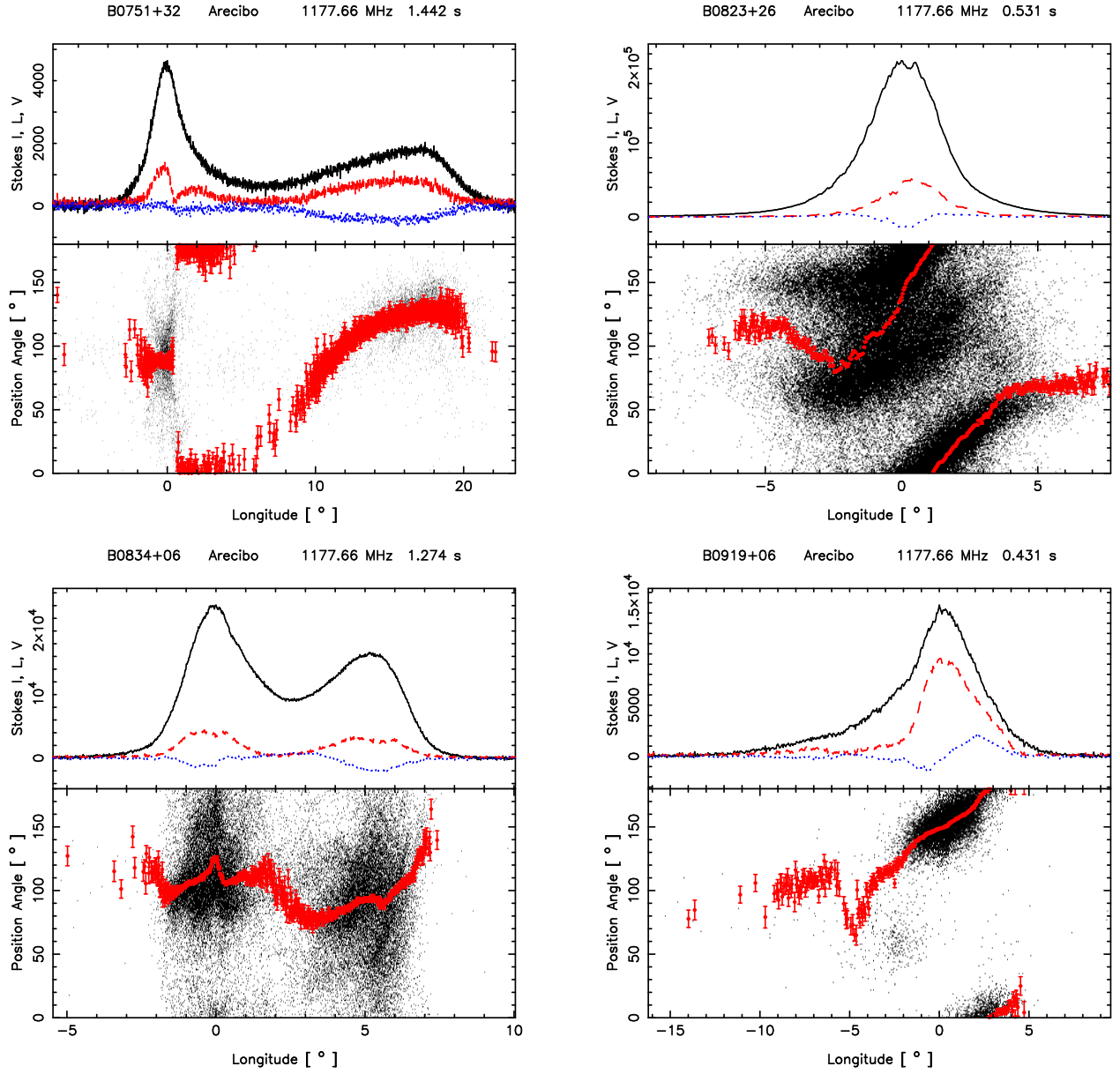
Fig. A6.— PPA histograms as in Fig. A2 for pulsars B0751+32, B0823+26, B0834+06 and B0919+06 observed with time resolutions of 59.5μsec.
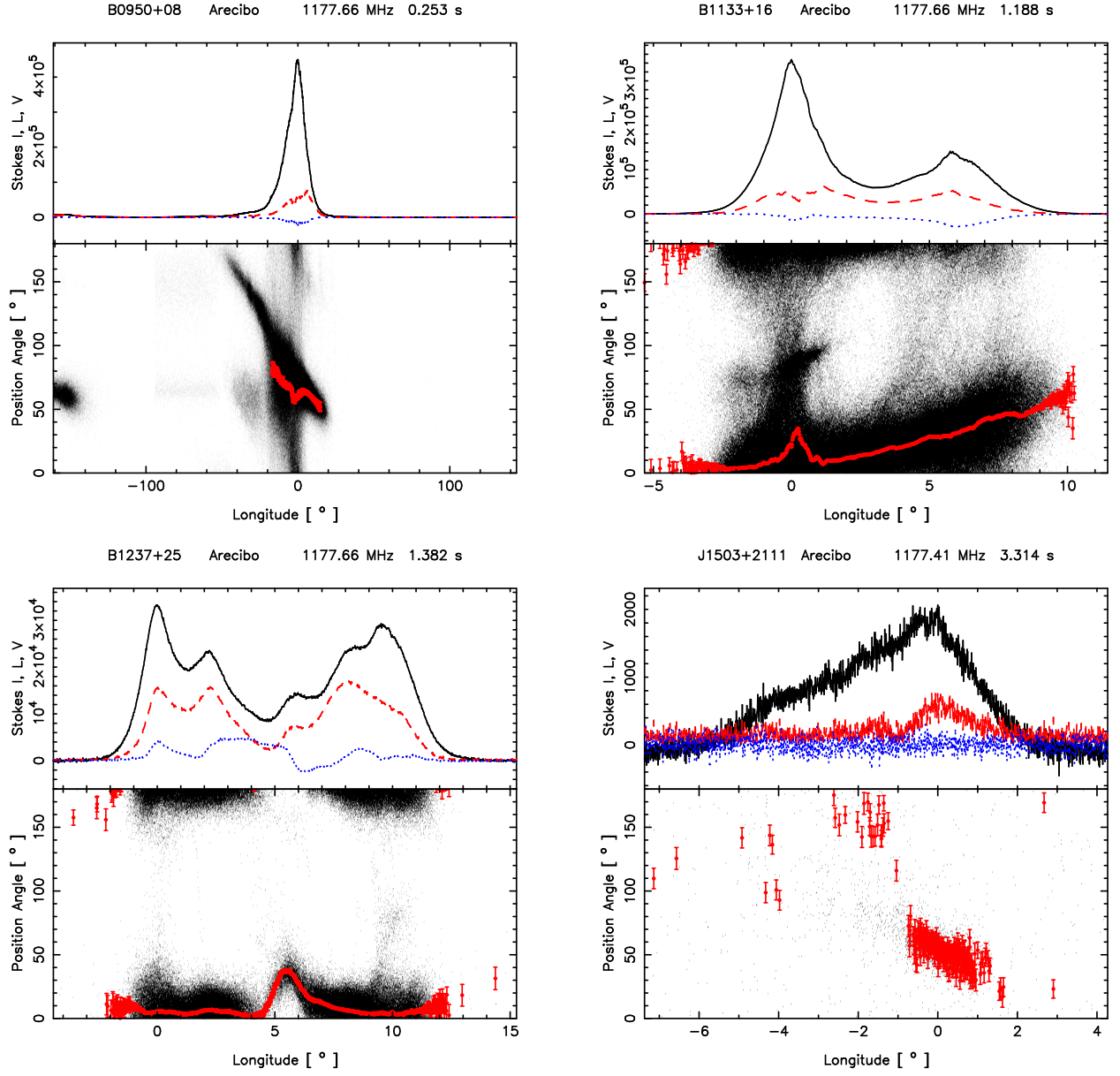
Fig. A7.— PPA histograms as in Fig. A2 for pulsars B0950+08, B1133+16, B1237+25 and B0919+06 observed with time resolutions of 59.5μsec.
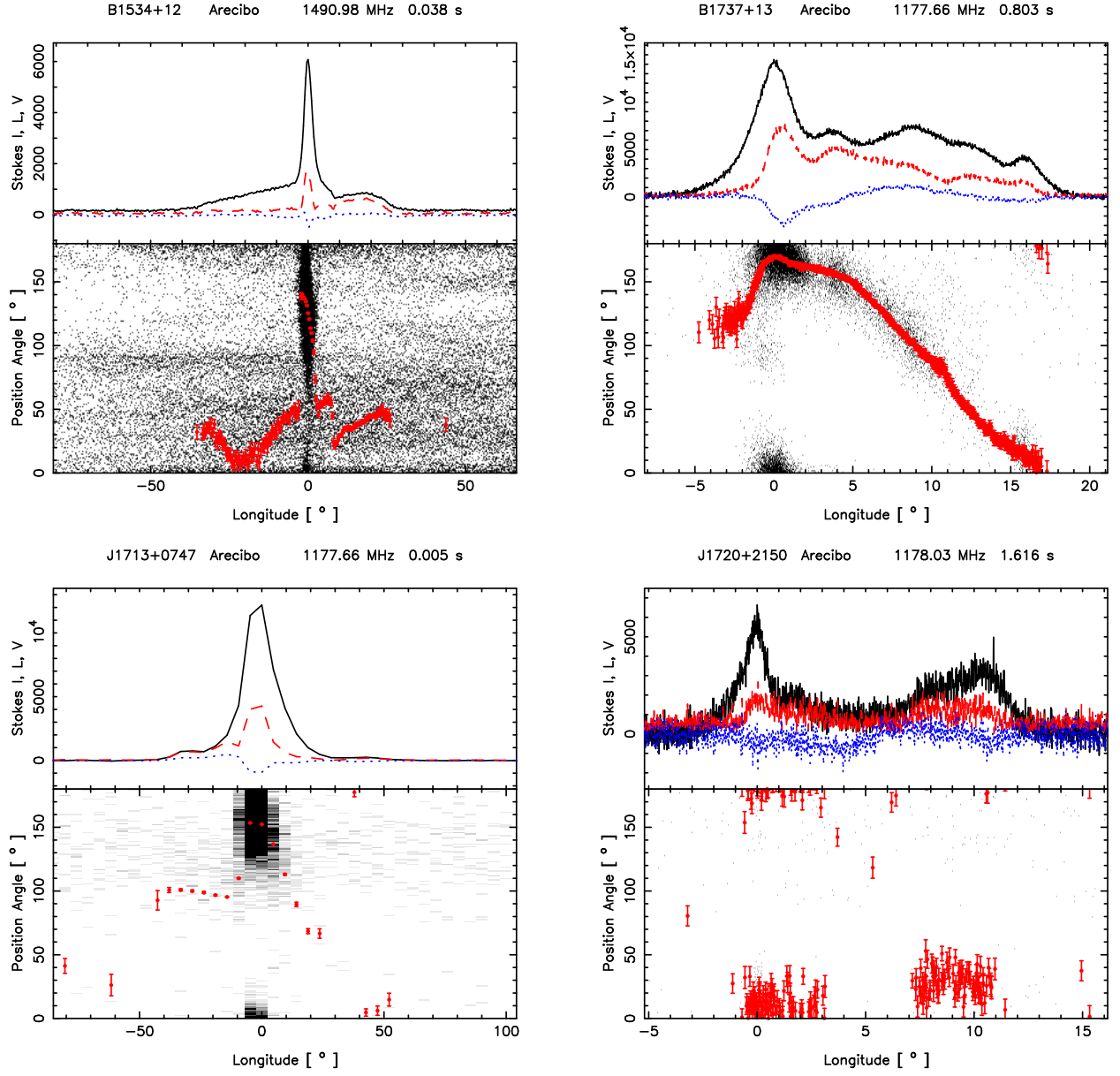
Fig. A8.— PPA histograms as in Fig. A2 for pulsars B1534+12, B1737+13, J1713+0747 and J1720+2150 observed with time resolutions of 59.5μsec.
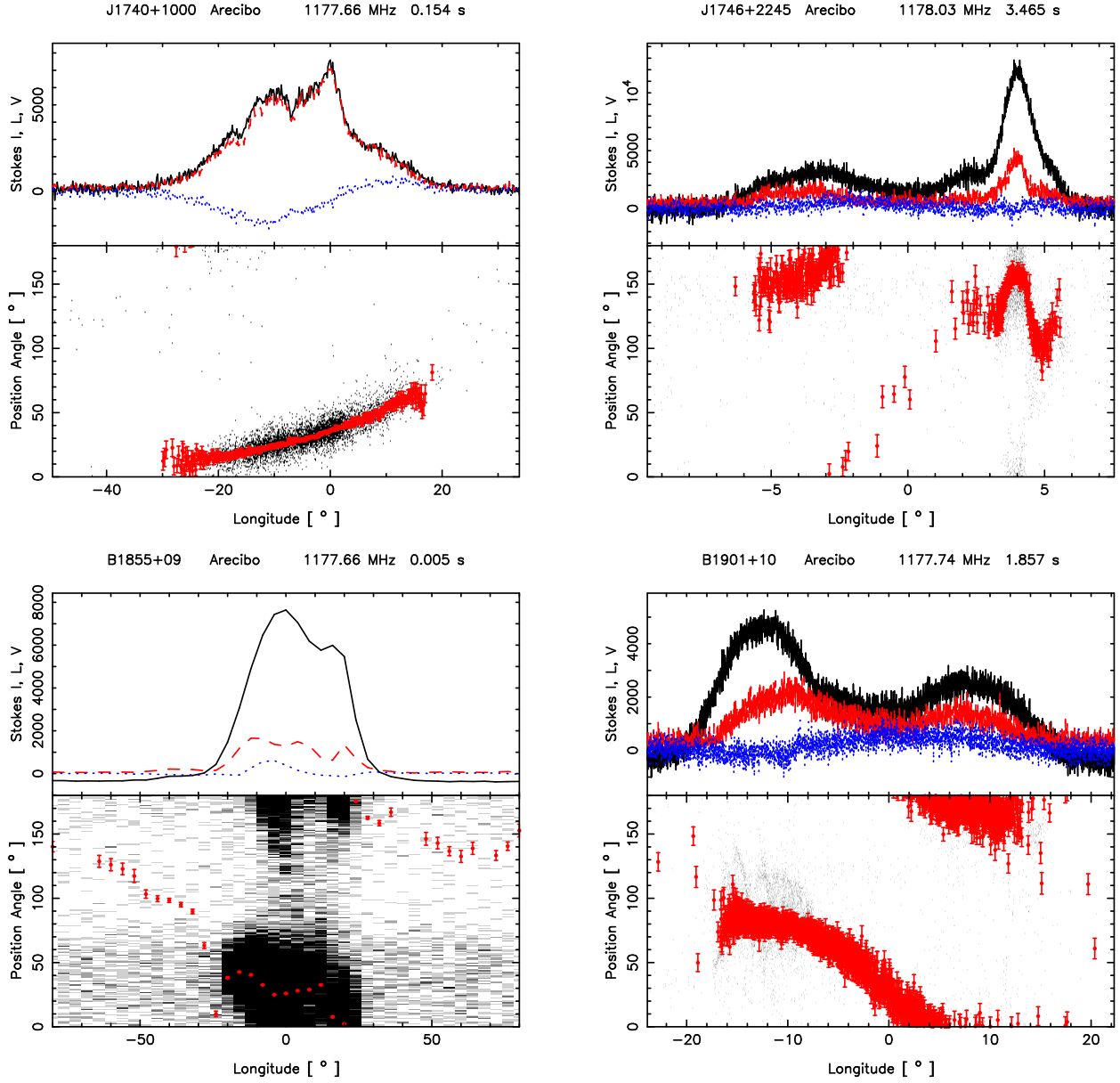
Fig. A9.— PPA histograms as in Fig. A2 for pulsars J1740+1000, J1746+2245, B1855+09 and B1901+10 observed with time resolutions of 59.5μsec.
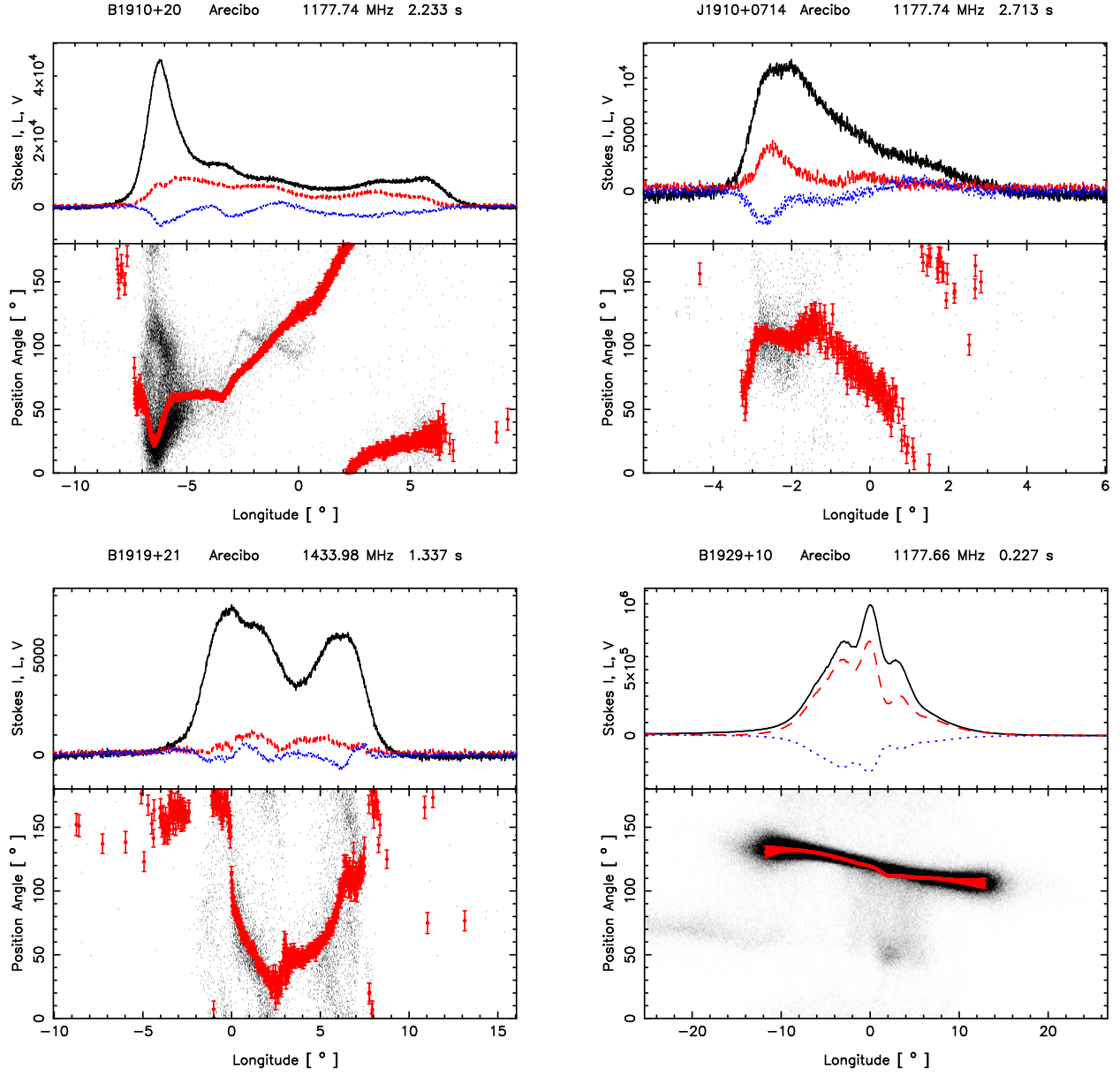
Fig. A10.— PPA histograms as in Fig. A2 for pulsars B1910+20, J1910+0714, B1919+21 and B1929+10 observed with time resolutions of 59.5μsec.
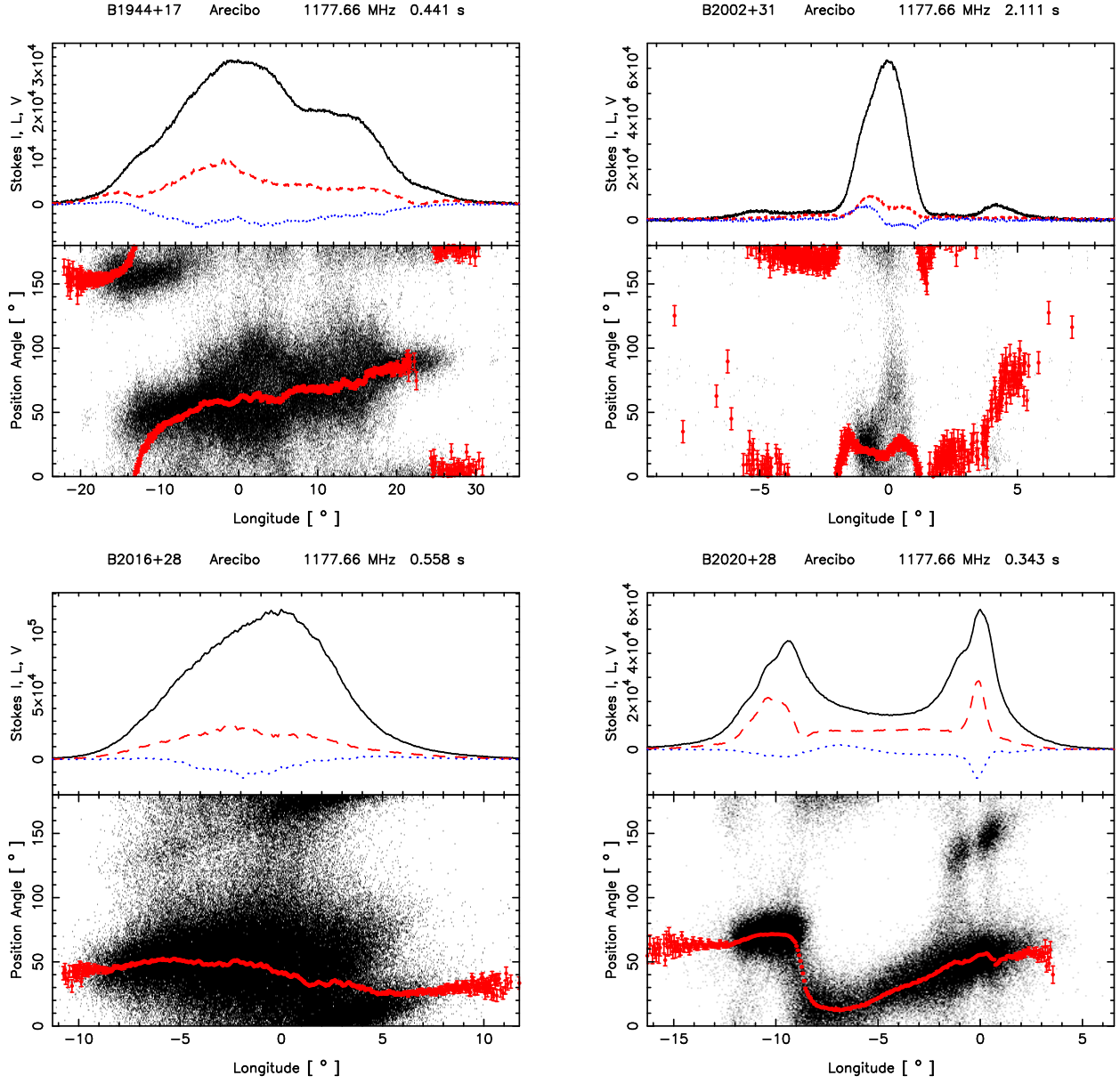
Fig. A11.— PPA histograms as in Fig. A2 for pulsars B1944+17, B2002+31, B2016+28 and B2020+28 observed with time resolutions of 59.5μsec.

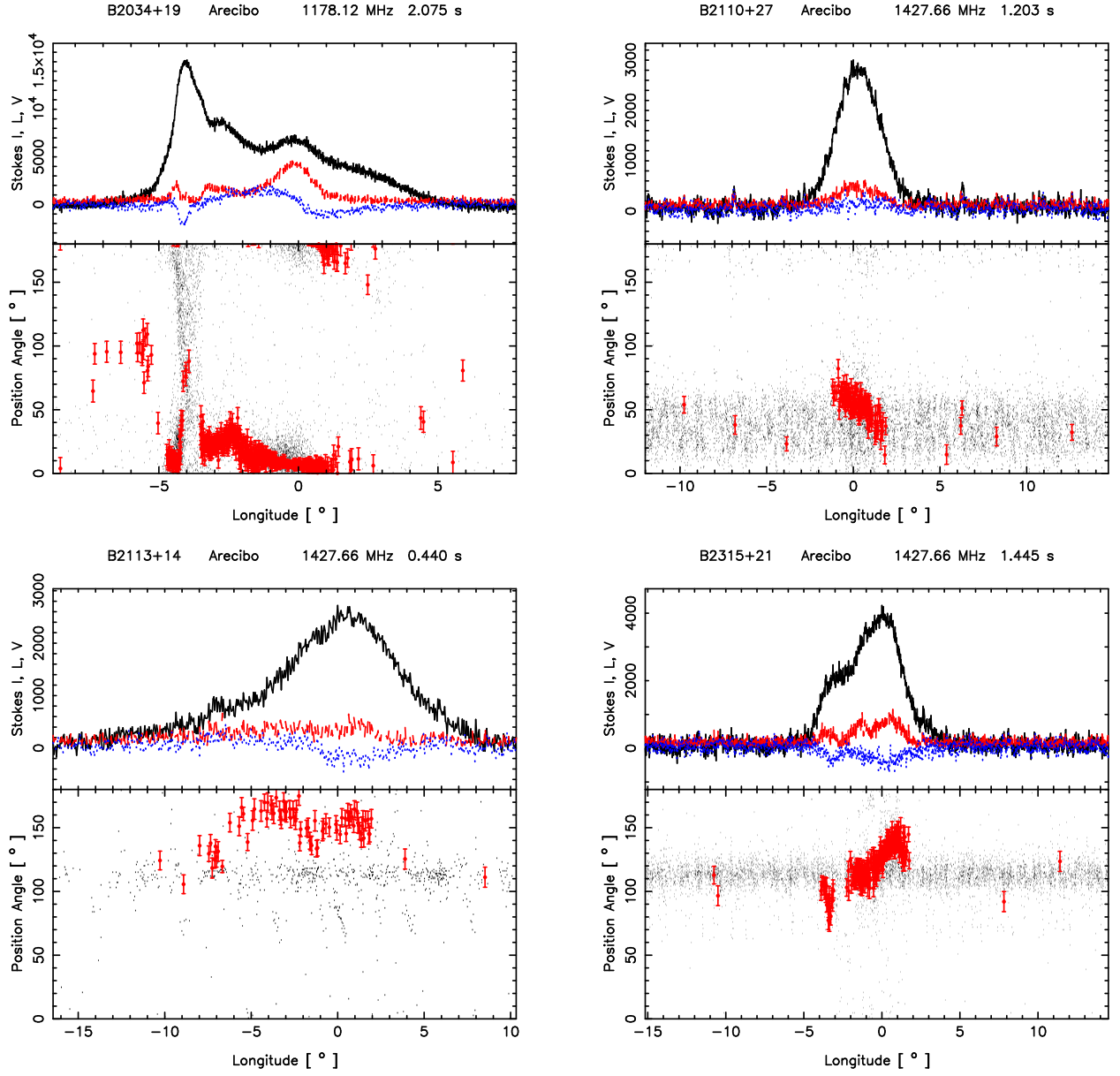Fig. A12.— PPA histograms as in Fig. A2 for pulsars B2034+19, B2110+27, B2113+14 and B2315+21 observed with time resolutions of 59.5μsec.